

Tuning Threshold Voltage in Organic Electrochemical Transistors by varying Doping of the Conjugated Polymer $p(g3T2-T)$

Marielena Velasco Enriquez

Thesis submitted for the degree of
Erasmus Mundus Master of Science
in Nanoscience and Nanotechnology,
graduation option Nanoelectronics

Supervisors:
Prof. Dr. Karl Leo
Prof. Dr. Steven De Feyter

Assessor:
PD Dr.rer.nat.habil. Hans Kleemann

Assistant-supervisor:
MSc. Anton Weissbach

© Copyright KU Leuven

Without written permission of the supervisors and the author it is forbidden to reproduce or adapt in any form or by any means any part of this publication. Requests for obtaining the right to reproduce or utilize parts of this publication should be addressed to Faculteit Ingenieurswetenschappen, Kasteelpark Arenberg 1 bus 2200, B-3001 Leuven, +32-16-321350.

A written permission of the supervisors is also required to use the methods, products, schematics and programmes described in this work for industrial or commercial use, and for submitting this publication in scientific contests.

Preface

Marielena Velasco Enríquez

Contents

Preface	i
Abstract	iv
List of Figures	v
List of Tables	vi
List of Abbreviations and Symbols	viii
1 Introduction	1
2 Background	3
2.1 Organic Semiconductors	3
2.1.1 Electronic Structure and Transport	3
2.1.2 Molecular Doping	4
2.2 Organic Mixed Ionic/Electronic Conductors (OMIECs)	6
2.2.1 Processes in OMIECs	8
2.3 Organic Electrochemical Transistors	10
2.3.1 Device Physics	10
2.3.2 Operation Modes	11
2.3.3 Important Figures of Merit	14
2.3.4 Side Reactions	17
3 Experimental Methods	19
3.1 Materials	19
3.2 Equipment	20
3.3 Software	21
3.4 Photomask	22
3.5 Experimental Procedure	22
3.5.1 Preparation of Films	22
3.5.2 Doping Characterization of Films	23
3.5.3 Doping in Organic Electrochemical Transistors	24
3.5.4 Fabrication of Solid Organic Electrochemical Transistors	28
4 Results and Discussion	31
4.1 Doping Characterization	31
4.1.1 Thickness, Sheet Resistance, and Resistivity	31
4.1.2 Absorbance measurements	32
4.1.3 Workfunction	33

4.2	Doping in Organic Electrochemical Transistors	34
4.2.1	Influence of Doping on OECT Channel	35
4.2.2	Stability of Undoped and Doped p(g3T2-T)	38
4.2.3	Counteracting Oxidation by Electrochemical De-doping	41
4.3	Fabrication of Solid Organic Electrochemical Transistors	43
4.3.1	Undoped Drop-casted SSE	44
4.3.2	Undoped Photopatterned SSE	45
4.3.3	Undoped Inkjet-Printed SSE	49
4.3.4	Doped Inkjet-Printed SSE	49
4.3.5	Threshold Voltage Shift in OECTs	52
5	Conclusions and Outlook	55
A	Absorption of p(g3T2-T) Doped with F6TCNNQ	57
B	Correlation of Cyclic Voltammetry and Transfer Characteristics	59
C	PEDOT:PSS vs Doped p(g3T2-T) as Channel	61
	Bibliography	63

Abstract

Organic Electrochemical Transistors (OECTs) exhibit advantageous properties, such as high transconductance and steep-slope switching, while operating at very low voltages. Although, their switching speed is comparatively slower than solid-state devices, it remains sufficient for applications in bioelectronics [1]. The gold standard conjugated polymer for p-type OECTs is PEDOT:PSS. However, its main drawback lies in its depletion-mode operation, which requires power to turn off the device. To minimize power consumption and improve stability, efforts have been made to the design conjugated polymers that allow accumulation-mode devices. One such polymer, 3-(2-(2-methoxyethoxy)ethoxy)thiophene (p(g3T2-T)) has demonstrated negative threshold voltages close to zero and high transconductance [2]. Furthermore, by doping p(g3T2-T) at various levels and drop-casting it as a gate, it has been possible to fine-tune the threshold voltage [3]. This study aims to adapt a microstructuring method for fabricating side-gated OECT devices that comprise different doping levels of F₄TCNQ and F₆TCNNQ in p(g3T2-T) and a solid-state electrolyte [4], the latter is deposited by inkjet printing. Additionally, the study aims to adjust the threshold voltage by utilizing these varying doping levels, while analyzing the stability and performance of the doped devices.

List of Figures

2.1	Energy level diagram of organic semiconductors	3
2.2	Degenerate and non-degenerate conjugated polymers	4
2.3	Scheme of doping processes in organic semiconductors	5
2.4	Representation of bipolaron formation introduced via doping	5
2.5	Formation of polaron, bipolaron, and bipolaron band	6
2.6	Material classes of OMIECs	7
2.7	Electronic transport mechanisms in OMIECs	8
2.8	Ionic transport mechanisms in OMIECs	9
2.9	Device physics of MOSFET vs OECT	10
2.10	Typical OECT structure and circuit model	11
2.11	Depletion- and accumulation-mode OECTs	12
2.12	Chemical structure of polymer g2T-T	13
2.13	Chemical structure and transconductance of g2T-T with side-chain engineering	13
2.14	OECTs benchmark with different OMIECs	15
2.15	Tuning of threshold voltage with different levels of doping p(g3T2-T)	16
2.16	Energy levels of neutral state of OMIECs related to oxygen reduction reactions potentials	18
3.1	Used photomask for fabricated OECT gold electrodes.	22
3.2	Chemical structures of the repeat units of p(g3T2-T) and F ₄ TCNQ dopant.	23
3.3	Dynamic spin-coating process to obtain undoped and doped films of p(g3T2-T).	23
3.4	Visualization of the workflow for Au-contacts patterning.	25
3.5	Visualization of the workflow for patterning undoped p(g3T2-T).	25
3.6	Visualization of the workflow for patterning doped p(g3T2-T).	26
3.7	Representation of experimental setup for measuring threshold voltage shift of a single OECT under ambient conditions. Scheme is not drawn to scale.	27
3.8	Chemical structures of the repeat units of p(g3T2-T) and F ₆ TCNNQ dopant.	27
3.9	Solid-OECT fabrication with undoped p(g3T2-T)	29
3.10	Solid-OECT fabrication with doped p(g3T2-T)	30
4.1	Color shift upon doping level increase	31

LIST OF FIGURES

4.2	Sheet resistance and resistivity drop upon doping	32
4.3	Absorbance spectra of different doping levels of p(g3T2-T)	33
4.4	Representation of the Fermi level shift upon doping	34
4.5	Micrographs of a patterned channel and gate p(g3T2-T) at different doping levels	35
4.6	Transfer characteristics and transconductance at different doping levels and V_{DS}	37
4.7	Transfer characteristics comparing different doping levels	38
4.8	Threshold shift at different doping levels and V_{DS}	39
4.9	Drain current over time of undoped-p(g3T2-T) coupled with SSE precursor	40
4.10	Transfer characteristics after electrochemical de-doping	40
4.11	Electrochemical de-doping of oxidized p(g3T2-T) OEET	42
4.12	Transfer characteristics and cyclic voltammograms of device using Ag/AgCl gate under ambient conditions	43
4.13	Performance of solid-OEET with drop-casted SSE	45
4.14	Performance of solid-OEET with photolithographed SSE	47
4.15	Performance of solid-OEET with photolithographed SSE in ambient conditions	48
4.16	Performance of solid-OEET with printed SSE	50
4.17	Inhomogeneous doping issues	51
4.18	Performance of solid-OEET with doped-p(g3T2-T)	52
4.19	Threshold voltage shift of all studied devices	53

List of Tables

2.1	Volumetric capacitance (C*) of various OECTs channel materials	14
3.1	Cyclic Voltammetry parameters.	21
3.2	Electrochemical Impedance Spectroscopy parameters.	22
3.3	Composition of the solid-state electrolyte [4].	26
3.4	Composition of adhesion promoter.	28
4.1	Sheet resistance and resistivity values for undoped and doped films of p(g3T2-T) with F ₄ TCNQ.	31
4.2	Calculated workfunction from UPS measurements and represented in Figure 4.4.	33
4.3	Maximum transconductance values extracted from Figure 4.6	36
4.4	Threshold voltage extracted from Figure 4.10	41
4.5	Parameters extracted from the characterization of drop-casted SSE OECTs	46
4.6	Parameters extracted from the characterization of photopatterned SSE OECT under N ₂ environment.	46
4.7	Parameters extracted from the characterization of photopatterned SSE OECT under ambient conditions	48
4.8	Parameters extracted from the characterization of printed SSE OECT .	49
4.9	Parameters extracted from the characterization of doped-p(g3T2-T) OECT	53

List of Abbreviations and Symbols

Abbreviations

OECT	Organic Electrochemical Transistor
V_{Th}	Threshold Voltage
p(g3T2-T)	
CV	Cyclic Voltammetry
EIS	Electrical Impedance Spectroscopy
UPS	Ultraviolet Photoelectron Spectroscopy
XPS	X-Ray Photoelectron Spectroscopy

Symbols

c	Speed of light
E	Energy
m	Mass
π	The number pi

Chapter 1

Introduction

The field of organic electronics has witnessed significant advancements in recent years due to its potential biocompatibility, mechanical compliant, and other application-specific characteristics. Among the numerous types of organic devices, Organic Electrochemical Transistors (OECTs) have attracted considerable attention due to their unique capabilities such as high transconductance and steep-slope switching at low operation voltages, which give them potential for use in energy storage, bioelectronics, and neuromorphic devices.

Accumulation-mode transistors, devices that are normally in the OFF state at zero-gate-biased condition, rely on the use of undoped conjugated polymers. In contrast, the ability to precisely control and tune the threshold voltage of an OECT can be achieved by manipulating the doping level of the mentioned conjugated polymer as shown by Tan et al. [3]. However, they fabricated devices that did not follow a complete microstructuring technique, limiting their integration into circuits.

The primary objective of this research is to address this missing information by developing a microstructuring method to fabricate accumulation-mode OECTs with controlled doping levels and enable their seamless integration into circuits. However, during the pursuit of this objective, it was identified that stability of the polymer and dopants in an electrochemical environment may pose challenges that need to be addressed as well. Therefore, this research project specifically aims to:

1. Characterize 3-(2-(2-(2-methoxyethoxy)ethoxy)ethoxy)thiophene (p(g3T2-T)) with varying doping levels of F₄TCNQ and F₆TCNNQ. This involves modifying the conjugated polymer film with different concentrations of dopant and analyzing their electronic structure, morphology and electrical properties using techniques such as UV-Vis spectroscopy, Ultraviolet Photoelectron Spectroscopy (UPS), Van Der Pauw method, Electrical Impedance Spectroscopy (EIS) and Cyclic Voltammetry (CV),
2. fabricate OECT devices, which involves utilizing the conjugated polymer at different doping levels, and adapting an existing method that combines electrode patterning techniques, spin-coating, photolithography and inkjet printing. The devices will be carefully optimized to ensure reproducibility and stability,

1. INTRODUCTION

3. assess doped polymer stability in OECTs, which involves performing conductivity measurements over time and selecting an electrolyte composition that allows a stable performance, and
4. investigate the shift in threshold voltage through electrical characterization of the fabricated OECT devices with varying doping levels of F₄TCNQ and F₆T₂CNNQ.

The thesis is structured as follows: Chapter 1 provides an overview of organic electronics and the importance of the OECT threshold voltage, and outlines the motivation, goals, and structure of the thesis. Chapter 2 presents a comprehensive review of the relevant background information on Organic Semiconductors (OSCs), Organic Mixed Ionic Electronic Conductors (OMIECs), and Organic Electrochemical Transistors, and relevant research on tuning the threshold voltage of OECTs. Chapter 3 illustrates the Experimental Methods used in this research, describes the materials, equipment, software, and procedures to chemically dope the films and characterization method employed in the study. Finally, it outlines the fabrication and characterization process of OECT devices. In Chapter 4, the experimental results obtained are presented, from the characterization of the conjugated polymer at different doping levels and fabricated OECT devices. Analysis of the relationship between the doping level and the shift in threshold voltage. Finally, it discusses the implications of the findings and their relevance to the field. Lastly, Chapter 5 provides a summary of the research objectives and the extent to which they were achieved, suggests future research direction, and potential applications.

Chapter 2

Background

2.1 Organic Semiconductors

Unlike inorganic semiconductors, organic semiconductors are lightweight, easy to chemically tune, mechanically flexible, and offer low-cost and low-temperature processing. All of these characteristics are responsible for the increased attention to this type of material in the field of organic electronics.

2.1.1 Electronic Structure and Transport

Organic semiconductors are π -conjugated molecules that comprise mostly carbon and hydrogen atoms, with alternating double and single bonds (sp^2 hybridization). The wavefunction of the sp^2 orbitals overlap so that electrons are delocalized. Based on the size of the conjugated system, organic semiconductors can be divided into conjugated polymers and small molecules. The latter have the advantage that their synthesis and low molecular mass allows to obtain them high purity material [5].

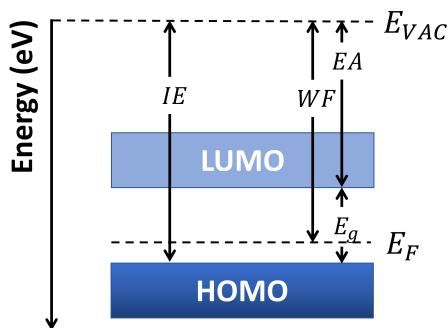


Figure 2.1: Energy level diagram of an p-type doped organic semiconductor.

The energy structure of organic semiconductors comprises a highest occupied molecular orbital (HOMO) state and a lowest unoccupied molecular orbital (LUMO) state, which are analogous to the valence and conduction bands, respectively, from inorganic semiconductors. The difference between these energy levels corresponds to

2. BACKGROUND

the energy gap (E_g) of the material, as illustrated in Figure 2.1. Additionally, we can define i) the Fermi level (E_F) using the material's work function (WF), ii) the ionization energy (IE), also referred as ionization potential (IP), using the HOMO energy, and iii) the electron affinity (EA), using the LUMO energy.

Organic semiconductor materials can also be classified based on whether their ground state is degenerate or non-degenerate. In the former case, the term “degenerate” describes monomers that have equivalent energy states in the ground state. In contrast, in the latter case, the ground state exhibits non-degeneracy, which is commonly observed due to the energy difference of aromatic (benzoid) and quinoid structures [6], as exhibited in Figure 2.2.

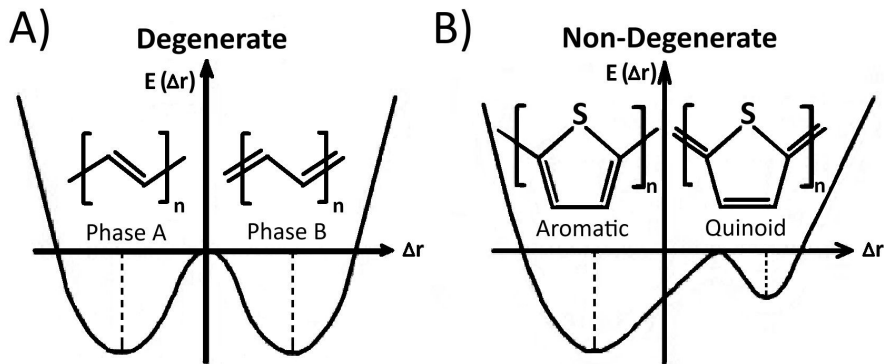


Figure 2.2: Potential energy change (electronic plus lattice distortion energy) in A) degenerate and B) non-degenerate ground-state-conjugated polymers. Extracted from reference [7].

In electronic transport theory for organic semiconductors, the concept of polarons is introduced. This quasiparticle effectively captures the alteration of the bond-length alternation pattern induced by the movement of charge carriers (electrons or holes) [8]. This alteration can be observed, for instance, when transitioning from Phase A to Phase B in degenerate molecules, or from aromatic to a quinoid structure in non-degenerate molecules.

2.1.2 Molecular Doping

The basic principles of molecular doping are similar than in inorganic materials. A donor or acceptor entity is added to generate electrons or holes, as shown in Figure 2.3. While n-type dopants donate electrons to the LUMO state, the p-type dopants extract electrons from the HOMO state, thus creating holes [9]. In other words, the Fermi level E_F of the polymer will shift towards the LUMO (or HOMO) level when there is n-type (or p-type) doping. This shift can be quantified using spectroscopy techniques such as Ultraviolet Photoelectron Spectroscopy (UPS) [10], although it may be somewhat limited by the penetration depth of the exciting electrons.

When doping occurs, the formation of a new quasiparticle named bipolaron occurs. For instance, if p-type dopants are introduced to a degenerate molecule (as

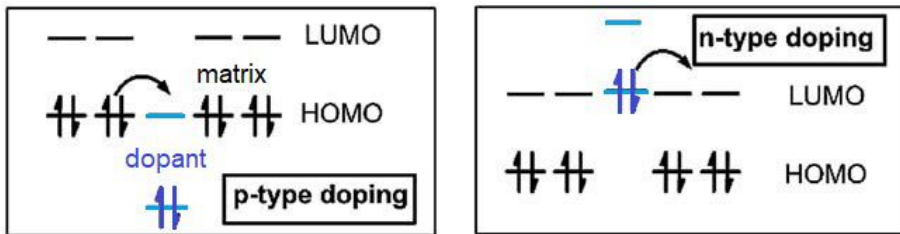


Figure 2.3: Schemes for p-type (left) and n-type (right) doping processes.

depicted in Figure 2.4), electrons are removed from double bonds. Focusing on a single event, this removal leaves one carbon positively charged, with an adjacent carbon atom possessing an unpaired electron. This unpaired electron moves along the polymer chain until it encounters another unpaired electron from a separate doping event. When they come together, they form a double bond, resulting in the creation of two charged polarons: a bipolaron [11].

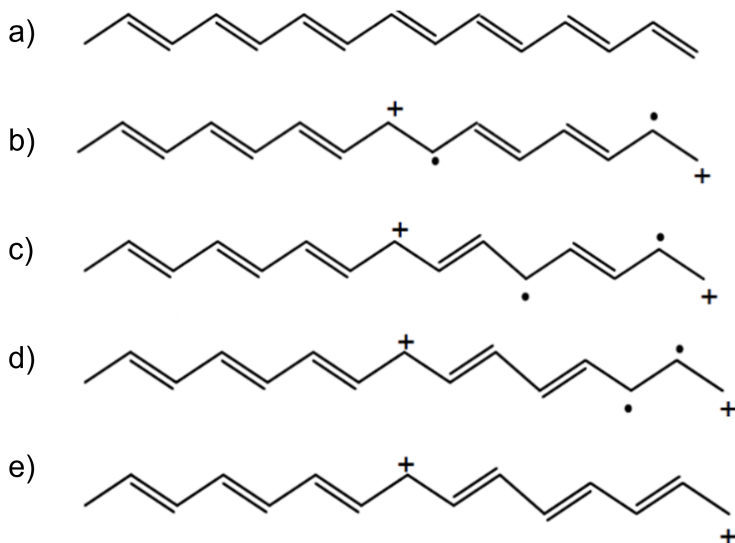


Figure 2.4: a) Structure of degenerate molecule. b) Electron extraction via doping. c) Unpaired electron shifting down. d) Unpaired electrons meet. e) Formation of double bond and two charged polarons: bipolaron.

The energy levels generated upon the formation of polarons and bipolarons in non-degenerate molecules are illustrated in Figure 2.5. As the doping density increases, the amount of bipolaron states also increases. Their overlapping leads to the formation of bipolaron bands, and the energy difference between the two in-gap states i and i^* , as shown from Figure 2.5b to d, decreases.

In addition to these new electronic states, the doped polymer will also exhibit distinct optical transitions that could be revealed through UV-Vis-NIR spectroscopy. In this technique, absorption peaks indicate the presence of these optical transitions.

2. BACKGROUND

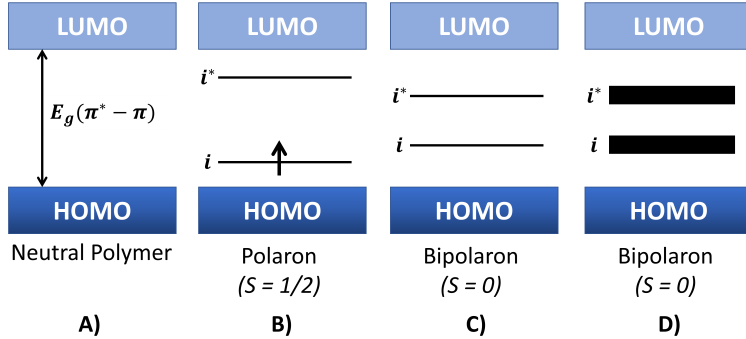


Figure 2.5: Potential energy change of aromatic and quinoid in the non-degenerate ground-state A) neutral conjugated polymer, and formation of B) polaron, C) bipolaron, and D) bipolaron bands upon doping. Extracted from reference [7].

However, these transitions may not be precisely quantified or clearly defined [7].

The use of small molecules as dopants for organic materials is commonly reported. Some strong acceptor (or electron-deficient) molecules that are widely used include 2,3,5,6 tetrafluoro-7,7,8,8-tetracyanoquinodimethane ($F_4\text{TCNQ}$) or 1,3,4,5,7,8 hexafluoro-7,7,8,8-tetracyanonaaphthoquinodimethane ($F_6\text{TCNNQ}$), both of which are also relevant to this work. The latter exhibits a higher electronic affinity (-5.3 eV) than $F_4\text{TCNQ}$ (-5.2eV), indicating that it can abstract electrons more efficiently, specially from polymers with low ionization potential ($\text{IP} < 5\text{eV}$) [12].

Among the various methods of molecular doping for conjugated polymers, Jacobs et al. conducted a comparison between solution-mixed and solution-sequential doping of P3HT, a thiophene-based polymer, doped with $F_4\text{TCNQ}$. These doping methods are considered straightforward and easy, especially when compared to other techniques such as vapor-phase doping [13]. Their research showed that solution-mixed films tend to have considerably rougher surface than solution-sequential films, which can negatively impact their conductivity [14]. The fact that solution-sequential doped films exhibit better homogeneity also makes them more compatible with microstructuring processes such as photolithography. Reason why it is going to be used in this work and will be further detailed in Section 3.5.1. However, this advantage comes at the expense of having less control over the doping levels when compared to solution-mixed films [15].

2.2 Organic Mixed Ionic/Electronic Conductors (OMIECs)

Organic Mixed Ionic/Electronic conductors are a class of organic semiconductors that allow the conduction of electrons (or holes) and ions. This feature sets them apart from other organic semiconductors. Commonly designed with polar side chains, OMIECs have been identified as a promising class of materials for the field of bioelectronics [16]. Initially investigated for batteries and super-capacitors [17] [18],

2.2. Organic Mixed Ionic/Electronic Conductors (OMIECs)

where the primary objective was to induce charges in a semiconducting polymer, OMIECs have rapidly expanded their scope to include other applications, among them, our focus: OECTs.

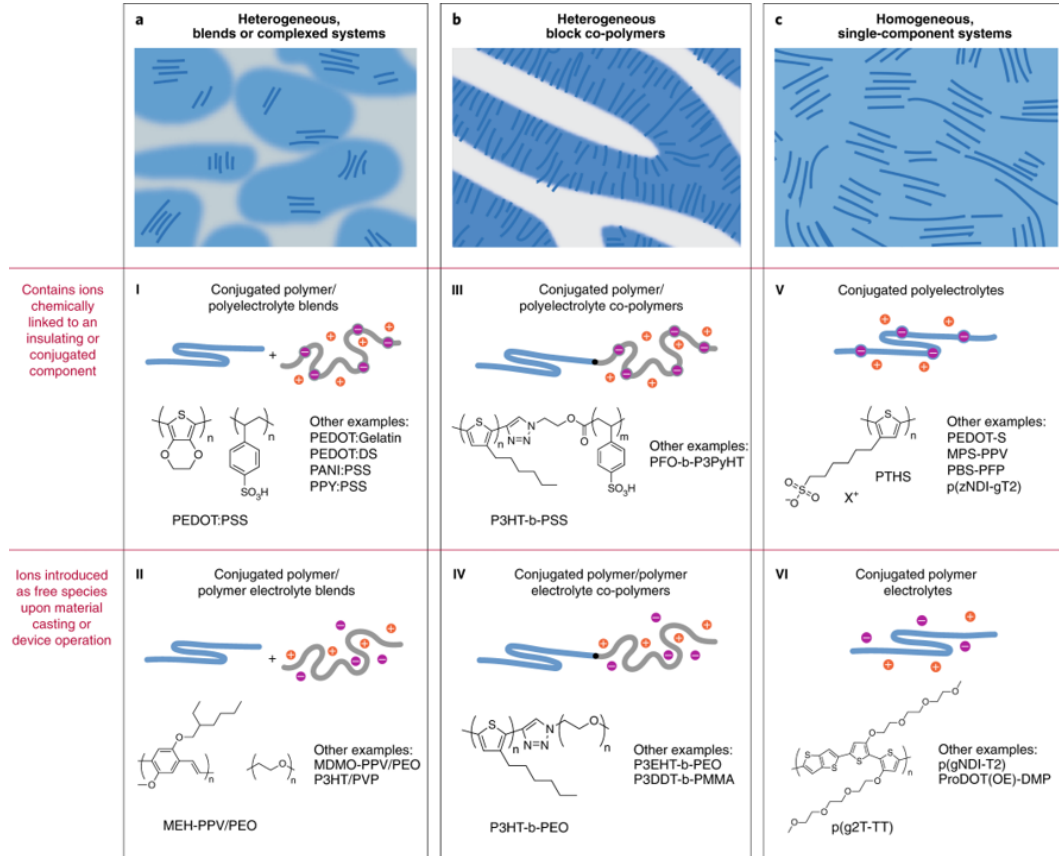


Figure 2.6: OMIECs classes. a) Heterogeneous blends of a conducting conjugated polymer with (I) a polyelectrolyte or (II) an ion-solvating polymer electrolyte. b) Heterogeneous block copolymers of a conducting conjugated polymer with (III) a polyelectrolyte or (IV) an ion-solvating polymer electrolyte. c) Fully conjugated (V) polyelectrolytes and (VI) ion-solvating polymer electrolytes. Extracted from reference [19].

Paulsen et al. classified OMIECs into six different categories based on whether they “*intrinsically contain ionic charge*” (I, III, V) or not (II, IV, VI), the latter group comprises materials that “*contain polar moieties that can solvate ions*”. Another distinguishing factor among these categories is whether the conjugated system is composed of a single material (homogeneous, type V and VI) or a two-component, more complex systems or block co-polymer materials (heterogeneous, type I, II, III, IV)[19]. A schematic representation is shown in Figure 2.6.

2. BACKGROUND

2.2.1 Processes in OMIECs

2.2.1.1 Ionic-electronic interactions

The presence of electronic charges in OMIECs requires also the presence of excess ionic charge, so charge in the system remains in balance. In the case of types II, IV, and VI OMIECs, a phenomenon known as stabilizing electrochemical doping is achieved through the presence of mobile ions that act as free charges. Conversely, other types of OMIECs have these stabilizing charges chemically bound and fixed, making them inherently doped.

The degree of coupling between electronic charges and excess ionic charges in OMIECs can be modulated by applying a bias when connected through an electrolyte [19]. This fundamental principle forms the basis of OECTs, which will be discussed further in Section 2.3.

2.2.1.2 Electronic transport

Electronic charge transport mechanisms present in OMIECs include thermally-activated hopping and band-like transport, as depicted in Figure 2.7. These mechanisms are not different from those observed in other conjugated polymers.

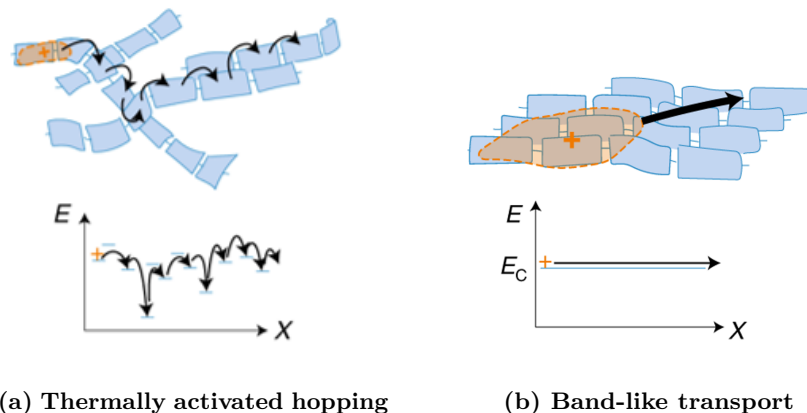


Figure 2.7: Schematic representation of electronic charge transport mechanisms: a) Thermally-activated hopping transport and b) band-like transport, where the electronic charge carrier is relatively localized and delocalized, respectively. Extracted from reference [19].

Thermally-activated hopping, as its name implies, is driven by thermal energy and is limited by the degree of structural disorder. In this mechanism, weakly-bonded electrons in delocalized π -orbital move along adjacent π -orbitals within the length of the conjugated polymer, or even between molecules where there is sufficient π - π overlapping. This mechanism predominates when there is a low electronic charge carrier density and a low density of accessible hopping states, resulting in low mobility and electrical conductivity [19].

In contrast, band-like transport typically occurs in OMIECs with increasing doping levels. In this case, the activation energy of charge hopping decreases, and carrier mobility increases. This leads to diffuse band-like charge transport within the polymer-stacking [20].

2.2.1.3 Ionic transport

While transport of anions and cations in OMIECs shares some similarities with the transport of electrons and holes, it is a more complex process, since ions can be “*multi-valent, and form pairs and larger clusters; moreover, they are sensitive to solvent and solvation*” [19].

Ion transport in dry OMIECs of type I, III, and V is unipolar because these ions are fixed on a polyelectrolyte. In contrast, in type II, IV, and VI OMIECs, both anions and cations are mobile. When OMIECs come into contact with an electrolyte, they tend to swell, allowing the penetration of excess ions from the electrolyte. Therefore, both mobile anions and cations contribute to ion transport to ensure electroneutrality.

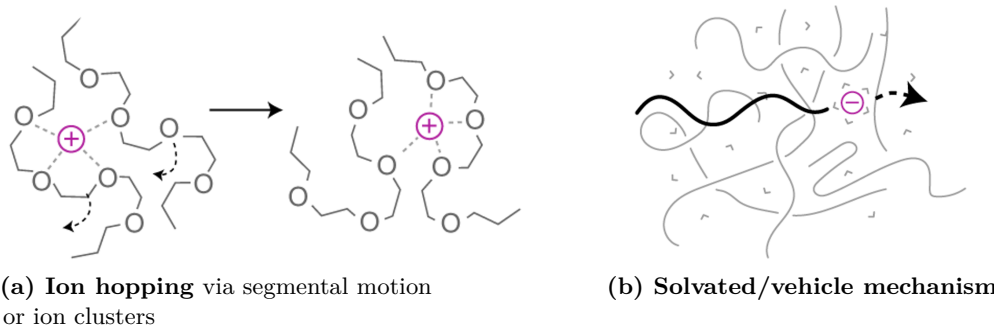


Figure 2.8: Schematic representation of ionic charge transport mechanisms: a) Ion hopping via segmented motion and b) vehicular solvated-ion transport. Extracted from reference [19].

There are two types of ionic charge transport in OMIECs: ion hopping and vehicular solvated-ion transport. In dry or minimally hydrated OMIECs, ion hopping assisted by segmental motion of the OMIEC side chains or backbone is the primary mechanism, as shown in Figure 2.8A. However, when OMIECs are in contact with a solvent or liquid electrolyte, both mechanisms are present, with solvated ion vehicle transport being the predominant mode. For instance, in water-based electrolytes, proton diffusion occurs via the Grotthuss mechanism, where protons within water molecules diffuse through neighboring molecules. This involves a transfer of ionic effects through the hydrogen-bonded network, as shown in Figure 2.8b.

Due to the existing ionic-electronic coupling, both ionic and electronic transport in OECTs and other OMIEC-electrolyte-based applications are not independent but are rather complex and must consider side effects such as hydration and electrolyte swelling [19], as will be further discuss in Section 2.3.

2. BACKGROUND

2.3 Organic Electrochemical Transistors

Organic Electrochemical Transistors are composed of metallic source, drain and gate electrodes, an organic conjugated polymer channel (specifically an OMIEC as described in previous sections), and an electrolyte that bridges the channel and the gate, as illustrated in Figure 2.10a. OECTs are devices that have received increasing attention due to their mechanical compliance, biocompatibility, and sensitivity to biochemical signals [21].

2.3.1 Device Physics

Although the structural configuration of OECTs differs from conventional metal-oxide-semiconductor field-effect transistors (MOSFETs), understanding the operation of the latter can provide insight into how OECTs function. In contrast to MOSFETs, where an insulator is used, OECTs are coupled with an electrolyte, as shown in Figure 2.9. When a gate voltage is applied, instead of polarizing the dipoles in the insulator and creating a field that causes accumulation of carriers at the interface of the semiconductor/insulator, as is the case with MOSFETs, in OECTs, the gate voltage drives ions to penetrate the bulk of the channel. Consequently, accumulation of carriers occurs throughout the whole volume of the OMIEC film. This mechanism explains the large gate-channel capacitance observed in these devices compared to MOSFETs and why the drain current takes into account a volumetric capacitance [22].

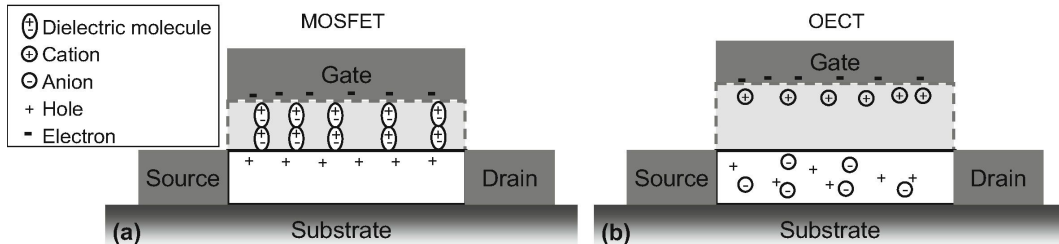


Figure 2.9: Comparison of p-type a) MOSFET and b) OECT, where the light-gray region represents an insulator and electrolyte, respectively. Extracted from reference [22]

Bernards and Malliaras implemented a model based on a p-type depletion-mode OECT (based on PEDOT:PSS as it is widely studies and fabricated material, further discussion in the following section) [23]. The model divides the behavior of the OECT into two circuits: an electronic circuit (comprising the source-channel-gate structure) and an ionic circuit (comprising the gate-electrolyte-channel structure).

The electronic circuit is treated as a *variable* resistor and is thus modeled using Ohm's law. Its variability arises from the fact that when a positive gate voltage is applied, de-doping of the semiconductor occurs, which is analogous to the compensation doping observed in silicon. Cations from the electrolyte penetrate the polymer, compensating for an acceptor.

Meanwhile, the ionic circuit consists of a resistor that represents the flow of ions in the electrolyte, connected in series with a capacitor representing the storage of ions in the channel, as shown in Figure 2.10b [1][23].

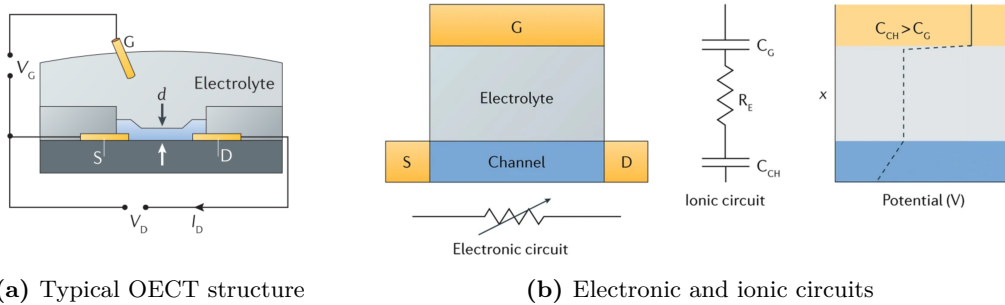


Figure 2.10: a) Typical structure of an organic electrochemical transistor. b) (Left) Electronic circuit modelled as a resistor with a variable resistance. (Right) Ionic circuit consisting of channel (C_{CH}) and gate (C_G) capacitors, coupled with a resistor corresponding to the electrolyte (R_E). Extracted from reference [1].

Finally, the drain current I_D for the steady state behavior of the OECT can now be described using the following equation:

$$I_D = \begin{cases} -\mu C^* \left[\frac{Wd}{L} \frac{V_{GS} - V_{Th}^2}{2V_{Th}} \right] & |V_{DS}| < |V_{GS}| - |V_{Th}| \\ -\mu C^* \frac{Wd}{L} \left[1 - \frac{V_{GS} - 1/2V_{DS}}{V_{Th}} \right] V_{DS} & |V_{DS}| > |V_{GS}| - |V_{Th}| \end{cases} \quad (2.1)$$

where μ is the charge mobility, C^* is the volumetric capacitance and W , d and L are the width, thickness and length of the channel. V_{GS} , V_{DS} and V_{Th} correspond to the gate, drain and threshold voltage, respectively. Parameters will be further discuss in Section 2.3.3.

2.3.2 Operation Modes

Analogous to conventional MOSFETs, depending on whether the device requires a gate potential to be turned ON, OECTs exhibit two operation modes: depletion and enhancement (the latter often referred to as accumulation in the context of OECTs). The operation modes are closely linked to the nature of the channel material.

As illustrated in Figure 2.11a and b, the polymer can be either intrinsically doped (conductive) or undoped (insulating). In the first scenario, the OMIEC already possesses anions that induce charges within its backbone. Consequently, to turn off the device, cations need to be injected to counteract this effect. Conversely, for an insulating polymer channel, a zero-gate biased OECT will have no charges induced in its backbone, resulting in the OFF state. To transition to the ON state, a gate voltage is required to drive anions into the polymer and induce charges.

2. BACKGROUND

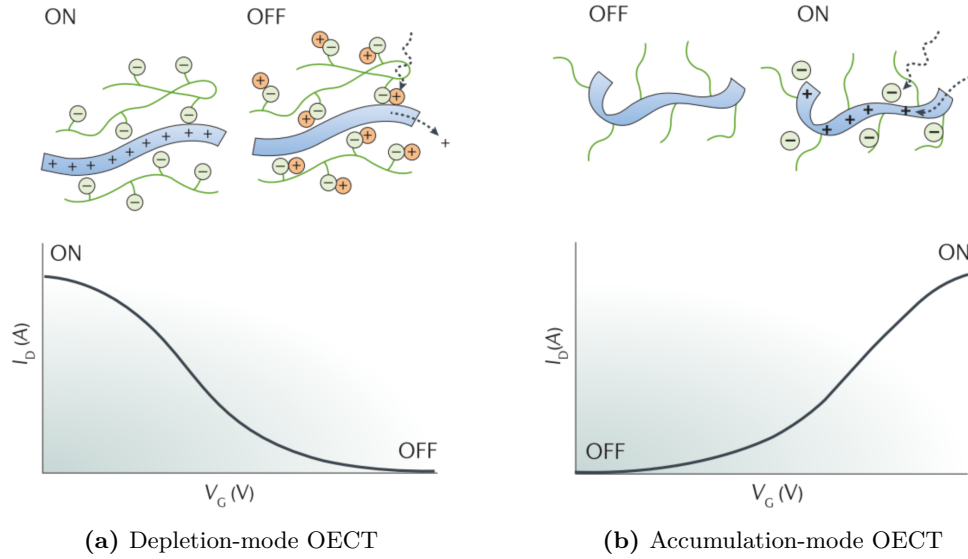


Figure 2.11: a) Transfer curve showing depletion-mode operation of a p-type OEET with a conducting polymer channel. b) Transfer curve showing accumulation-mode operation of a p-type OEET with a insulating polymer channel. Images extracted from reference [1].

2.3.2.1 Standard material for depletion-mode OECTs

Poly(3,4-ethylenedioxythiophene) poly(styrene-sulfonate) (PEDOT:PSS) is a “*degenerately doped*” [23] or conductive polymer that is widely used in various applications in organic electronics. Classified as type I OMIEC, as seen in Figure 2.6, it is a blend between a conjugated polymer (PEDOT) and a polyelectrolyte (PSS), the latter possesses chemically linked ions and serves as a polymeric acid template to allow dispersable suspensions [19].

Due to its commercial availability, operational stability, and relatively high performance, PEDOT:PSS became a standard material for p-type OECTs. However, its main drawback lies in its depletion-mode operation.

With the aim of minimizing power consumption, there is a strong interest in fabricating high-performance accumulation-mode devices [2][15][24][25]. These devices offer the advantage of dissipating less static power when the device is not in operation, due to low OFF current [16].

2.3.2.2 Prospective materials for accumulation-mode OECTs

PEDOT:PSS has not been ruled out as a possible accumulation-mode OECT, Keene et al. employed a series of amines to de-dope PEDOT:PSS and achieve OECTs with negative turn-on voltages [25]. However, synthetically modifying PEDOT:PSS in a controlled manner remains a challenge.

In parallel to these efforts, researchers are also working on the design of new conjugated polymers with the aim of not only having accumulation-mode OECTs but enhancing their performance. Nielsen et al. reported a series of semiconducting polymers with triethylene glycol (TEG) side chains, some of which demonstrated good performance. Among the five thiophene- and benzodithiophene-based polymers, they found out that the one with a backbone consisting of 2,2'-bithiophene (blue) polymerized with other thiophene molecule (green), named as **g2T-T**, as seen in Figure 2.12, exhibited the highest performance [2].

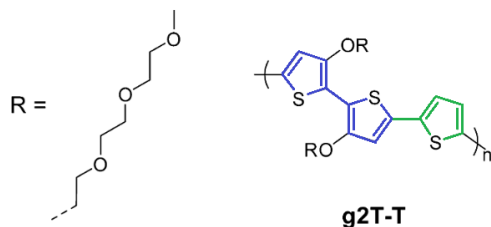


Figure 2.12: Chemical structure of polymer with backbone g2T-T, R representing the side chain. Extracted from reference [2].

Moser et al. conducted a study using the same backbone (g2T-T) to investigate the impact of the length of the ethylene glycol (EG) side chain on the performance of OECTs [26]. They found that reducing the side chain length maximized both the capacitance and mobility of the OECTs. However, a shorter side chain is less favorable for ion-polymer interaction.

Their research suggested an optimum-side-chain length of 3 monomers, compared to 2, 4 and 6 monomer. OECTs based on 3-(2-(2-methoxyethoxy)ethoxy)ethoxy thiophene (p(g₃T₂-T)) exhibited a turn-on voltage close to zero and superior performance compared to other thiophene-based species (as seen in Figure 2.13 and Table 2.1), even surpassing PEDOT:PSS-based OECTs [24].

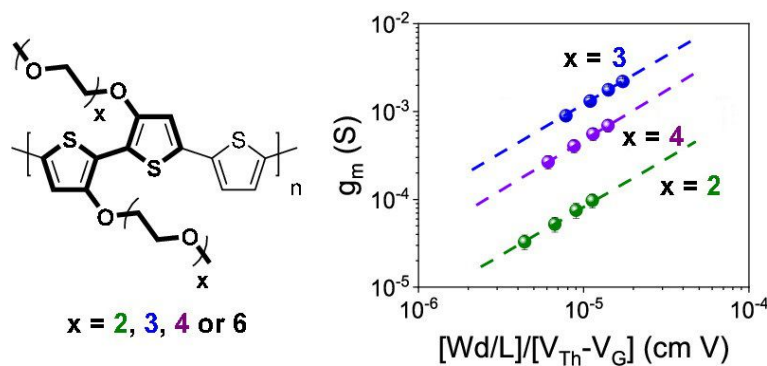


Figure 2.13: (Left) Chemical structure of the repeat units for p(gxT2-T). (Right) Transconductance vs channel geometry and operating parameters of p(gxT2-T) for x = 2, 3 and 4. Extracted from reference [26].

2. BACKGROUND

The structure of the polymer was designed to have a backbone that warrants reversibility during electrochemical redox reactions and good electronic transport, while the side chains enhance its stability in aqueous electrolytes and facilitate efficient transport of both ionic and electronic charge carrier [27].

Under the classification presented in Figure 2.6, p(g3T2-T) can be categorized as a type VI OMIEC that consists of a conjugated polymer with ions introduced as free species. Whereas, PEDOT:PSS contains ions that are chemically linked to the polyelectrolyte (PSS). This structural distinction results in p(g3T2-T) displaying larger magnitudes of ionic-electronic coupling and volumetric capacitance compared to biphasic OMIECs like PEDOT:PSS [19]. Understanding these structural characteristics is crucial for addressing the challenges associated with achieving stable OEETs, as it will be further addressed in this thesis.

Polymer	C^* (Fcm^{-3})	Reference
p(g2T2-T)	8±2	[26]
p(g3T2-T)	211±18	[26]
p(g4T2-T)	192±10	[26]
PEDOT:PSS	39	[24]

Table 2.1: Volumetric capacitance (C^*) of OEETs channel materials including p(g2T2-T), p(g3T2-T), p(g4T2-T) and PEDOT:PSS using a 0.1 NaCl electrolyte and Ag/AgCl pellet electrode.

2.3.3 Important Figures of Merit

2.3.3.1 Transconductance

Transconductance is considered as the most important parameter for measuring the amplification capability of any transistor. It is calculated as the first-order derivative of the output current (drain current) with respect to the input voltage (gate-source voltage), expressed as $g_m = \partial I_D / \partial V_{GS}$. Bernards and Malliaras derived this parameter in their mathematical model for depletion-mode p-type OEETs [23], as discussed in Section 2.3.1. When considering both n-type and p-type OEETs, the transconductance can be expressed as follows:

$$g_m = \frac{Wd}{L} \mu C^* |(V_{th} - V_G)|, \quad (2.2)$$

where W , L and d are the channel width, length, and thickness, respectively, μC^* denotes the product of mobility and volumetric capacitance, while V_G and V_{th} stand for the gate voltage and threshold voltage, which will be further discussed in the following subsections.

Typically, the maximum transconductance ($g_{m,max}$) is reported, which falls into the saturation regime. Inal et al. reported the maximum transconductance for various channel materials with different device geometry parameters. They used an Ag/AgCl pellet as reference/gate electrode and 0.1M NaCl as electrolyte. Their

results showed that OECTs with polymerized g2T backbones exhibited the best performance, achieving transconductance values ranging from 1 to 30 mS, depending on the geometry (Figure 2.14a) [24].

2.3.3.2 μC^* product

The parameter μC^* is considered the most important for benchmarking OECT channel materials because it represents both the ionic and electronic transport properties [24]. It is the product of two important parameters, μ , the electronic mobility, and C^* , the volumetric capacitance, the latter encloses the ion penetration, transport, and storage ability of the OMIEC film.

Along with the transconductance, Inal et al. determined the values of μC^* by calculating the linear slope of the maximum transconductance and channel geometry (Figure 2.14a), using Equation 2.2. They correlated their results with independent calculations of both parameters and found that polymerized g2T backbones exhibited the highest μC^* value of $261 \pm 29 F cm^{-1} V^{-1} s^{-1}$. Among the materials that showed a close 1:1 relationship for both methods of calculation of the μC^* product, polymerized g2T backbones stood out (Figure 2.14b) [24].

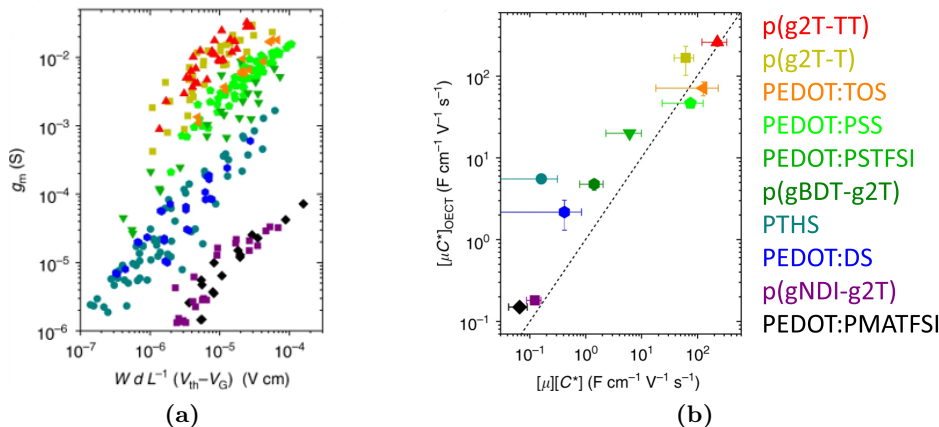


Figure 2.14: a) Plot of μC^* product calculated by the linear slope between transconductance and channel geometry. b) Calculated slope from a) in function of the product of independent determination of μ and C^* , dotted line represents the 1:1 relation between both methods of calculation. Extracted from reference [24].

Calculating the electronic mobility (μ) independently is challenging due to the presence of ionic species. This calculation is normally performed in transient regimes, taking advantage of ions' lower mobility, but it is outside the scope of this work.

One method to calculate the volumetric capacitance (C^*) is by performing Electrochemical Impedance Spectroscopy (EIS). Equation 2.3 is used to calculate the capacitance (C) based on the imaginary part of impedance (Z^{img}) at low frequency ranges where the capacitance should describe a plateau. The calculated capacitance is then divided by the film volume to obtain C^* [28].

2. BACKGROUND

$$C = \frac{1}{2\pi \cdot f \cdot |Z^{img}|}, \quad (2.3)$$

It is important to note that the capacitance (C) can be potential-dependent when electrochemical doping is modulated in OECTs with an applied bias [24].

2.3.3.3 Threshold voltage

The threshold voltage (V_{th}) in an OECT can be determined from the steady-state transfer characteristics (I_D vs V_{GS}). To calculate V_{th} , you can plot the square root of I_D as a function of V_{GS} and extrapolate the linear portion of the slope, where it intersects the x-axis. This value of V_{th} represents the “film’s readiness for ion penetration” in OECTs [28].

Controlling or shifting the threshold voltage is desirable, specially for integrating transistors into circuits to meet specific requirements for operation, noise margins, and power consumption. There are different approaches to achieve this. One approach is the chemical de-doping of PEDOT:PSS, as discussed in previous sections, which can shift the threshold voltage to negative values characteristic of accumulation-mode OECTs [25].

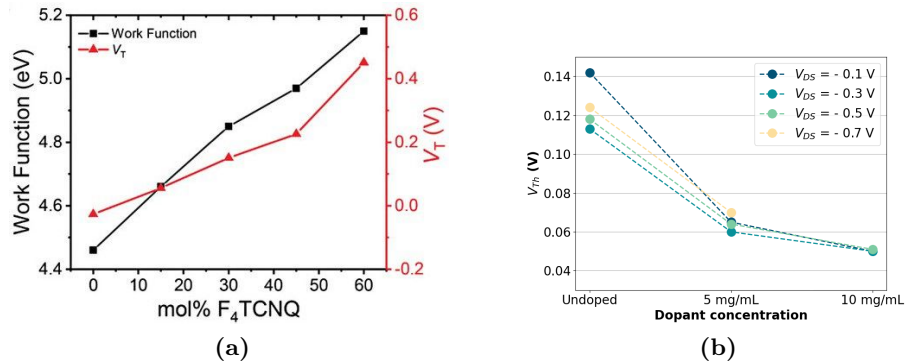


Figure 2.15: Controlling OECT threshold voltage by chemical doping of p(g3T2-T) gate electrode with F_4TCNQ . a) Plot of threshold voltage and gate work function for doped gates of different dopant concentrations. b) Transfer curves of p(g3T2-T) channel OECT with p(g3T2-T) gates of various F_4TCNQ dopant concentrations. Extracted from reference [3].

Another approach, explored by Tan et al., involves tuning the doping level of the gate to shift the threshold voltage. They used p(g3T2-T) and achieved a 400 mV change in threshold voltage with a 60% molar ratio of F_4TCNQ dopant, as shown in Figure 2.15. This approach offers advantages such as i) protecting the material from oxidation by bringing the Fermi level towards the highest occupied molecular orbital, and ii) avoiding interference with the channel which helps to maintain the transconductance unaffected [3].

2.3.4 Side Reactions

2.3.4.1 Water uptake and swelling

Water uptake and swelling are important side reactions that occur when OMIECs come into contact with water-based electrolytes. Even in the pursuit of solid-state OECTs, precursors may contain a certain degree of water content [4][29], making it necessary to understand the impact of water-related side reactions.

Water uptake in OMIECs causes an increase of mass (swelling) and changes in morphology. This water uptake occurs because OMIECs need to compensate for their intrinsic doping, and as a result, “*the effect of doping-induced hydration on the OMIEC morphology must be taken into account when designing OECTs*” [30].

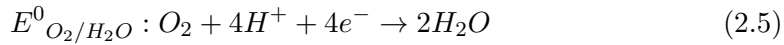
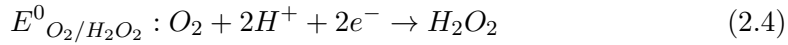
Savva et al. conducted a study to investigate the influence of water on the performance of PEDOT:PSS OECTs. They found that water uptake led to a 10-13% increase in mass under non-biased conditions. Interestingly, the concentration of water played a role in the ionic charging rate. While lower concentrations of water (NaCl_{aq} 10 mM, 100mM, 1M, and 6M) led to faster ionic charging, the fastest response time was achieved with NaCl_{aq} 1 M. This was attributed to attractive forces between counter ions, which hindered the drift of anions and delayed the injection of ions from the electrolyte [31].

Another study by Savva et al. showed that a certain level of hydration is necessary for facile ionic transport, but can have a negative impact on electronic charge transport, particularly in glycol-based side chains [30]. These side chains are commonly used in accumulation-mode OECTs, where ionic transport is already enhanced through side-chain engineering [27].

2.3.4.2 Oxygen Reduction Reaction (ORR)

The Oxygen Reduction Reaction (ORR) is a common undesirable side reaction that occurs under environmental conditions, especially in devices fabricated with polymers having low ionization potential (IPs). The use of OMIECs with low IPs is frequent in accumulation-mode OECTs.

The ORR is a non-capacitive faradaic reaction that takes place between the OMIEC and molecular oxygen, involving electron-transfer. This reaction can yield either the oxidation (p-doping) of the OMIEC which acts as the catalyst, water (H_2O) or hydrogen peroxide (H_2O_2), as described in 2.5 and 2.4. While water was already discussed and is not detrimental, hydrogen peroxide, on the other hand, may accelerate device degradation and if immersed in biological environment, it can be harmful [16].



As represented in Figure 2.16, η_1 and η_2 represent the free energy difference between reactants and the reaction products H_2O_2 and H_2O , respectively. If this free

2. BACKGROUND

energy difference is negative, indicating that the reaction requires an energy input, the ORR is endergonic, while a positive free energy difference makes it exergonic (spontaneous). For instance, to prevent the formation of hydrogen peroxide, a polymer with higher IP ($> 4.9\text{eV}$) would be required.

In the context of OECTs, where polymers like PEDOT:PSS and p(g3T2-T) are used, it is crucial to recognize that these materials undergo exergonic reactions in the presence of oxygen. Consequently, the formation of hydrogen peroxide becomes inevitable. It becomes important to identify the operational points where the production of H_2O_2 becomes disproportional, particularly in applications where long-term reliability is essential. Managing and mitigating the effects of H_2O_2 formation will be a key consideration in the development of these devices.

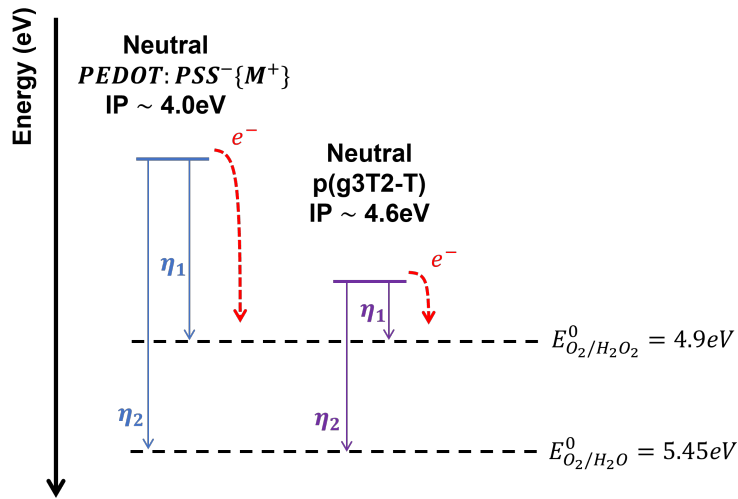


Figure 2.16: Simplified mechanism of two- and four-electron Oxygen Reduction Reactions with neutral states of OMIECs: p(g3T2-T) and PEDOT:PSS. The free energy difference between reactant and the reaction products is represented by η . Image adapted from reference [16], where values are defined from cyclic voltammetry measurements using Ag/AgCl as reference electrode and NaCl as electrolyte.

Chapter 3

Experimental Methods

3.1 Materials

All reactives were purchased from commercial suppliers.

- Chromium etchant: High purity ceric ammonium nitrate, Standard, Sigma Aldrich
- Gold etchant: HHPAA (2-Hydroxy-4'-(2-hydroxyethoxy)-2-methylpropiophenone), 98%, Standard, Sigma Aldrich
- Developer: AZ 726 MIF Developer, Merck performance Materials GmbH
- EG: Ethylene glycol, \geq 95%, Sigma Aldrich
- [EMIM][EtSO₄]: (1-Ethyl-3-methylimidazolium ethyl sulfate), \geq 95%, Sigma Aldrich
- MBBAm: (N,N'-Methylenebisacrylamide), 99%, Sigma Aldrich
- NIPAm: (N-Isopropylacrylamide), 97%, Alfa Aesar
- Sacrificial Layer 1: Sacrificial Layer 1 (SL1), Orthogonal Inc
- Photoresist: AZ 1518 Photoresist, Merck Performance Materials GmbH & Microchemical GmbH
- Photoresist for undoped species: NLOF 2020, commercial negative-tone photoresist, Microchemical
- Orthogonal Photoresist for doped species: OSCoR 4020 Photoresist, Orthogonal Inc.
- Developer for SL1: Developer HF 7300, Orthogonal Inc.
- Orthogonal Developer for OSCor 4020: Orthogonal Developer 103a, Orthogonal Inc.

3. EXPERIMENTAL METHODS

- Orthogonal Stripper: Orthogonal Stripper 900, Orthogonal Inc.
- p(g3T2-T): 3-(2-(2-methoxyethoxy)ethoxy)thiophene from Professor Iain McCulloch, Chemistry Research Laboratory, University of Oxford.
- Dopants: 1,3,4,5,7,8-hexafluorotetracyanonaphthoquinodimethane ($F_6\text{TCNNQ}$) and 1,3,4,5-tetrafluorotetracyanonaphthoquinodimethane ($F_4\text{TCNQ}$), 97%, Sigma Aldrich.
- Adhesion promoter: Silane A174 (3-(Trimethoxysilyl)propyl methacrylate), TCI.

3.2 Equipment

- Baking: All baking steps were carried out on a Stuart SD160 digital hotplate (Stuart Equipment, UK).
- Electrical characterization (ambient): Device characterization under ambient conditions was performed on a Everbeing C-6 Probe Station (Everbeing Int'l Corp., Taiwan), connected to a Keithley 4200-SCS Semiconductor Characterisation System (Keithley Instruments, USA).
- Electrical characterization (glovebox): Device characterization was performed in a nitrogen-filled glovebox. Probing needles were connected to two Keithley 236 Source Measure Units (Keithley Instruments, USA).
- Cyclic voltammetry and Impedance measurements: Measurements were carried out by using a Metrohm Autolab PGSTAT302N potentiostat/galvanostat (Metrohm AG, Switzerland).
- Micrographs: Micrographs were taken on a Nikon Eclipse LV100ND microscope, equipped with a DS-Fi2 camera (Nikon, Japan).
- Photolithography: Photolithography was carried out on a SÜSS Microtec MJB4 maskaligner system (SÜSS Microtec AG, Germany).
- Photomasks: Photomasks were custom made by Compugraphics Jena in a 4-inch format (soda-lime glass covered with chromium) and held several mask designs (Compugraphics Jena GmbH, Germany).
- Plasma cleaning: O_2 -plasma cleaning was performed by using a Harrick PDC-002 plasma cleaner (Harrick Plasma, USA), connected to a Leybold Heraeus Combitron CM 330 Vacuum Gauge Controller (Leybold GmbH, Germany).
- Plasma etching: O_2 -plasma etching was performed by using a Diener electronic ATTO plasma cleaner (Diener electronic GmbH & Co. KG, Germany).
- Profilometry: Profilometry was performed on a Veeco Dektak 150 surface profiler (Veeco Instruments Inc., USA).

- Film resistance measurements: The film resistance was measured using a linear four-point probe system (Lucas four-point probe connector) connected to a multimeter (Keithley 2010 Multimeter).
- Transmittance and Reflectance measurements: Measurements were performed with UV-Visible-NearInfraRed Spectroscopy on a SolidSpec-3700 UV-Vis-NIR spectrometer using an integral sphere from Shimadzu.
- Energy of HOMO/HBEC cutoff measurements: Measurements were done using Ultraviolet Photoelectron Spectroscopy (UPS) on a PHOIBOS 100 from Specs, a Helium plasma discharge lamp (UVS10/35, Specs).
- Spincoating: Samples were coated with a SAWATEC SM-180-BT spincoater (SAWATEC AG, Switzerland).

3.3 Software

- Data processing: All data was processed by customized scripts written in Python. Files import and manipulation was done by using OS [32] and CSV [33] modules. Mathematical computations (e.g. fits, integration) were carried out by employing the NumPy [34], SciPy [35], and PeakDetect [36] libraries. Visualisations were performed using the Matplotlib library [37]. All is compiled in the following GitHub Repository: **marivelasco25/Thesis.git**.
- Electrical characterization: Measurements were performed by controlling SMUs through the in-house developed SweepMe! software (<https://sweep-me.net/>).
- Profilometry: Profilometry was performed by using the Dektak software (Veeco Instruments Inc., USA).
- Cyclic voltammetry: Measurements were performed by using the NOVA software (Metrohm AG, Switzerland). Parameters were fixed and are described in the following table:

Parameter	Value
Start/Stop potential	0 V
Upper vertex potential	1 V
Lower vertex potential	-1 V
Number of scans	10
Scan rate	0.1 V/s

Table 3.1: Cyclic Voltammetry parameters.

- Impedance measurements: Measurements were performed by using the NOVA software (Metrohm AG, Switzerland) in potentiostatic mode. Parameters were fixed and are described in the following table:

3. EXPERIMENTAL METHODS

Parameter	Value
Initial frequency	10^5 Hz
Final frequency	10^{-1} Hz
Frequencies per decade	10
Amplitude (V_{RMS})	0.01 V

Table 3.2: Electrochemical Impedance Spectroscopy parameters.

3.4 Photomask

The employed photolithography mask for OECT fabrication depict a specific layout of gold electrodes, as illustrated in Figure 3.1. Detailed information about the photolithography process is provided in the following section.

This layout accommodates 14 devices, each with a channel length of 70 μm and a 20 μm overlap on both sides. The channel width is set at 190 μm . Additionally, the gate electrode dimensions describes a length of 190 μm and a width of 220 μm , with a gate-channel distance of 30 μm . All 14 devices will be located within a glass sample substrate measuring $2.5 \times 2.5 \text{ cm}^2$.

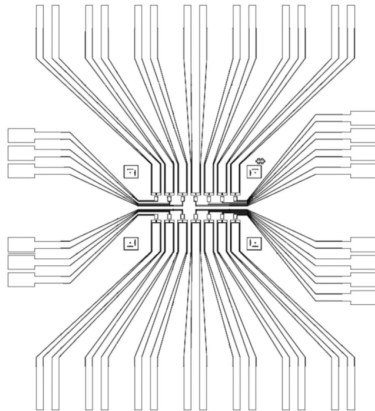


Figure 3.1: Used photomask for fabricated OECT gold electrodes.

3.5 Experimental Procedure

All fabrication steps were performed under standard cleanroom conditions.

3.5.1 Preparation of Films

Dynamic spin-coating of p(g3T2-T). In contrast to the approach described in reference [3], which employed drop-casting for the deposition of undoped and doped p(g3T2-T) films, our objective is to enable photolithography and facilitate a miniaturization process. To achieve this, uniform films are needed. The BioSens group members at IAPP had previously established dynamic spin-coating method

3.5. Experimental Procedure

due to the high volatility of p(g3T2-T) solvent, chloroform. Substrates were cleaned through sequential steps of ultrasonic bath in acetone for 15 minutes, IPA rinse, N₂ drying, and 5 minutes of O₂ plasma etching (0.3 mbar). Then, 70 μ L of 10 mg/mL of p(g3T2-T) mixed at 60°C for 20 minutes, was applied using dynamic spin-coating at 3000 RPM for 60s, yielding approximately 70nm thick films. The samples were then dried at 80°C.

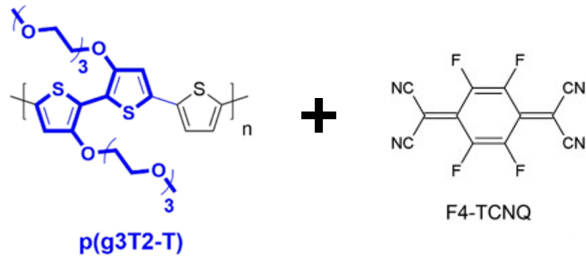


Figure 3.2: Chemical structures of the repeat units of p(g3T2-T) and F₄TCNQ dopant.

Dynamic spin-coating of F₄TCNQ dopant. Different doping levels of p(g3T2-T) were achieved by dynamic spin-coating 140 μ L of dopants at different concentrations (5, 10 and 20 mg/mL, as seen in Figure 3.3), previously mixed in acetonitrile at 60°C for 20 minutes. The samples were then dried at 80°C.

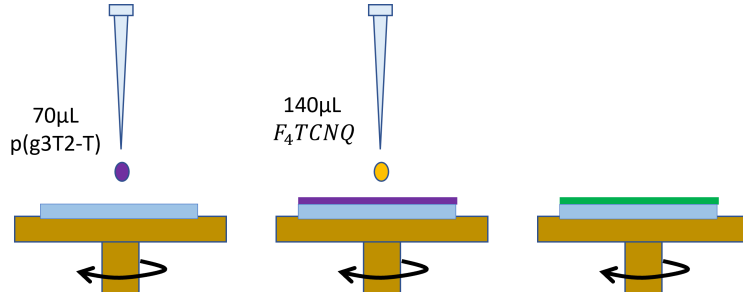


Figure 3.3: Dynamic spin-coating process to obtain undoped and doped films of p(g3T2-T)).

3.5.2 Doping Characterization of Films

Profilometer. The films were scratched 4 times to remove part of material, and measure the cavity depth to obtain the film thickness.

Four-point probe. A four-point probe was used to calculate the relation between induced voltage in inner probes and input current between outer probes. Then sheet

3. EXPERIMENTAL METHODS

resistance and resistivity were calculated using the Van Der Pauw method, following reference [38], via equations:

$$R_S = \frac{\pi}{\ln(2)} R = 4,53R \quad [\Omega/sq], \quad (3.1)$$

where R is the resistance measured with the four-point probe setup, and

$$\rho = R_s t \quad [\Omega.cm], \quad (3.2)$$

where t is the thickness of the film.

UV-Vis-NIR Spectroscopy. After the preparation of the films onto quartz substrates, transmittance (T) and reflectance (R) was measured using the UV-Vis-NIR Spectrometer in the range of 285 to 1600 nm. Then, absorption (A) was calculated via

$$A = 1 - T - R, \quad (3.3)$$

and normalized with respect to the incoming light [39]. Additional measurements were taken, after some days of storage under ambient conditions to check its stability in air.

Ultraviolet Photoelectron Spectroscopy. After the preparation of the films, the energy of the highest occupied molecular orbital cutoff (E_{HOMO}) and the high binding energy cutoff E_{HBEC} was measuring using UPS. The pressure in the chamber during measurements was about $5 \cdot 10^{-9}$ mbar, while the base pressure is in the range of $10 \cdot 10^{-10}$ mbar. The workfunction (WF) and ionization energy (IE) are calculated by using the following equations:

$$WF = h\nu - E_{HBEC} \quad [eV], \quad (3.4)$$

$$IE = h\nu - (E_{HBEC} - E_{HOMO}) \quad [eV], \quad (3.5)$$

where $h\nu = 21.22eV$, the main He I excitation line of the Helium plasma discharge lamp [40].

3.5.3 Doping in Organic Electrochemical Transistors

3.5.3.1 Influence of Doping on OECT Channel

Photolithographically patterned substrates with gold contacts for source, drain and gate were obtained using mask layout illustrated in Figure 3.1. The steps outlined in references [4] and [41] were followed, which is also represented in Figure 3.4.

Then p(g3T2-T) films were deposited following the procedure described in the previous section. The patterning of doped-p(g3T2-T) channel adopted a procedure similar to the one described in references [4][41], which involves the use of

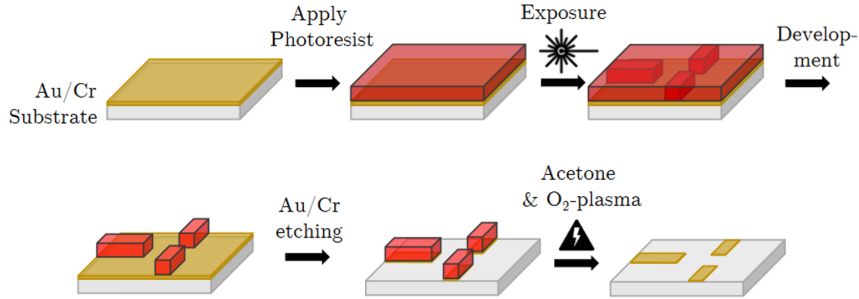


Figure 3.4: Visualization of the workflow for Au-contacts patterning. Image modified based on reference [41].

PEDOT:PSS. However, some modifications in the exposure and developing times were made. In contrast, the patterning of undoped-p(g3T2-T) samples, required a different protocol. A sacrificial layer is introduced to ensure proper cross-linking with photoresist. Both processes are detailed in the following:

Patterning undoped p(g3T2-T). Patterning of the p(g3T2-T) was achieved with photolithography, as shown in Figure 3.5. First, a fluoropolymer Sacrificial Layer 1 (SL1) was spin-coated at 6000 RPM for 60 s, followed by a baking step for 180 s at 113°C. Before the deposition of photoresist, a O₂ plasma cleaning step was applied for 60 s to promote adhesion. Then, NLOF 2020 photoresist was spin-coated at 3000 RPM for 60 s and baked for another 60 s at 113°C. Exposure of negative resist was performed for 12 s by shadowing all areas except the ones of interest. After post-baking for 60 s at 113°C, NLOF was developed by rinsing the sample in AZ MIF 726 for 20 s and wash off in DI water (carried out extra times if necessary). Next, SL1 was developed using HF 7300 developer for 45 s and spin rinsed at 3000 RPM (carried out extra times if necessary). Excess of p(g3T2-T) was removed by O₂-plasma etching for 180 s. The sample was placed in Orthogonal Stripper 900 overnight at room temperature, to complete the removal. Finally, ultrasonication in acetone was added for 15 min the next day.

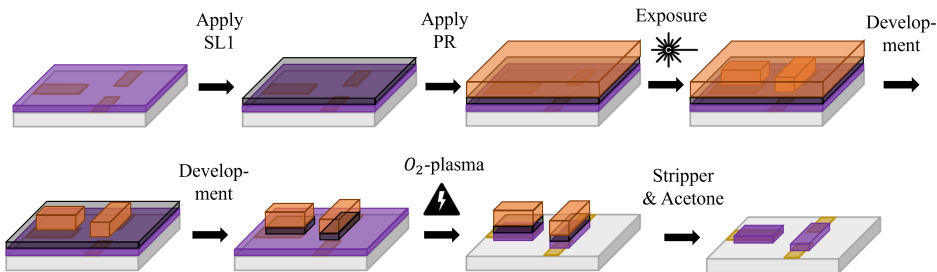


Figure 3.5: Visualization of the workflow for patterning undoped p(g3T2-T).

3. EXPERIMENTAL METHODS

Patterning doped p(g3T2-T). Patterning of the doped p(g3T2-T) was achieved with photolithography, as shown in Figure 3.6. First, the orthogonal photoresist OSCoR 4020 was spin coated at 3000 RPM for 60 s and baked for another 60 s at 103°C. Exposure of negative resist was performed for 20 s with shadowing all areas except the ones of interest, one extra cycle was added if using higher dopant concentration (10 mg/mL). After post-baking for 60 s at 103°C, OSCoR was developed using Orthogonal Developer 103a for 45 s and spin rinsed at 3000 RPM for 60 s (carried out extra times if necessary). Excess of doped-p(g3T2-T) was removed by O₂-plasma etching for 180 s. The sample was placed in Orthogonal Stripper 900 overnight at room temperature.

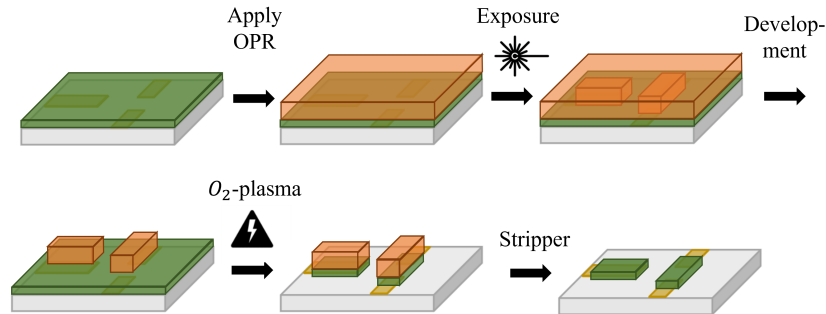


Figure 3.6: Visualization of the workflow for patterning doped p(g3T2-T).

OECT with undoped- and doped-p(g3T2-T) channel. A solid-state electrolyte precursor was prepared according to the details provided in Table 3.3. Next, 20 μ L of this precursor were drop-casted to the patterned samples, both undoped and doped, covering all 14 devices in the sample. Finally, a Ag/AgCl pellet was installed and used as gate (Figure 3.7). Transfer characteristics were measured under ambient conditions with a V_{GS} swept backwards from 1.0 V to -0.8 V.

Component	Amount	Function
H ₂ O	1.0 mL	dilution
[EMIM][EtSO ₄]	1.5 mL	ionic liquid
MBBAm	20 mg	crosslinker
NIPAm	750 mg	monomer
HHPAA	200 mg	photoinitiator
EG	1.5 mL	increase viscosity, ensures good print
Triton	1 drop	surfactant, ensures good print

Table 3.3: Composition of the solid-state electrolyte [4].

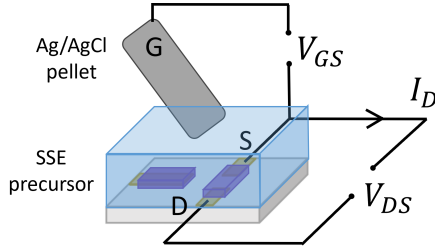


Figure 3.7: Representation of experimental setup for measuring threshold voltage shift of a single OECT under ambient conditions. Scheme is not drawn to scale.

3.5.3.2 Stability of Undoped and Doped p(g3T2-T)

Films of p(g3T2-T) doped with F₆TCNNQ were deposited and patterned, following same procedures described in subsection 3.5.1 and 3.5.3.1.

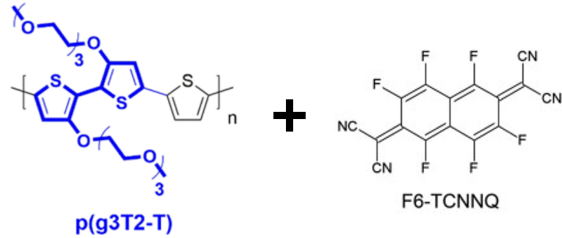


Figure 3.8: Chemical structures of the repeat units of p(g3T2-T) and F₆TCNNQ dopant.

Channel conductivity measurements. The channel conductivity of an undoped-p(g3T2-T) device was measured in N₂ then ambient conditions immediately after spin-coating onto substrate with patterned gold contacts. The channel conductivities of both doped and undoped devices were monitored after patterning process (as described in previous section) for two hours under N₂ environment, and for 1h30 under ambient environment. Finally, they were again monitored upon drop-casting solid-state electrolyte precursor.

Transfer characteristics. Transfer characteristics were measured at different V_{DS} (-0.5, -0.3, -0.1 V) of the undoped p(g3T2-T) device using a Ag/AgCl pellet as gate under environmental conditions, immediately after finalizing the process described above.

3.5.3.3 Counteracting Oxidation of Undoped p(g3T2-T) by Electrochemical De-doping

Channel conductivity measurements. Undoped p(g3T2-T) samples onto patterned-gold-contacts substrates were prepared. The solid-state electrolyte precursor was

3. EXPERIMENTAL METHODS

drop-casted onto the 14 devices, one device source-drain was negatively-biased and applied a positive gate voltage (+1 V). Channel conductivity was monitored.

Transfer characteristics. Transfer characteristics were measured at V_{DS} of -0.1 using the OMIEC gate under N₂ environment, immediately after process described above. Other measurements were performed after UV light exposure, and in ambient conditions using a Ag/AgCl pellet gate.

3.5.4 Fabrication of Solid Organic Electrochemical Transistors

3.5.4.1 Solid-OECTs using Undoped-p(g3T2-T)

After following the patterning steps for undoped-p(g3T2-T) from Subsection 3.5.3.1. Three different methods of applying the solid-state electrolyte precursor were tested. Then, transfer characteristics were measured at a constant V_{DS} of -0.1V, and a V_{GS} swept backwards from 1.0 V to 1.0 V at a scanning rate of 0.083 V/s. Cyclic voltammetry and electrochemical impedance spectroscopy were performed by short-circuiting source and drain to probe between channel and gate. Parameters were fixed as described in Section 3.3, and measurements were taken one day after the fabrication.

Application of adhesion promoter. An adhesion promoter, consisting of reactants detailed in Table 3.4, was applied to the substrate. The sample was placed in a Petri dish at 50°C and covered for 20 min. Subsequently, it was thoroughly rinse with ethanol and dried on a hot plate at 100°C for a minimum of 10 min. The composition and application steps of adhesion promoter was previously established by Biosens group members at IAPP.

Component	Amount
SilaneA174	30 μ L
Etanol	3mL
Acetic acid	60 μ L

Table 3.4: Composition of adhesion promoter.

OECT with drop-casted Solid-State Electrolyte. Solid-state electrolyte precursor was drop-casted and then exposed for 2 cycles of 60 s in a mask aligner, as shown in Figure 3.9a. No adhesion promoter was applied in this sample.

OECT with photopatternable Solid-State Electrolyte. After the application of the adhesion promoter, the solid-state electrolyte precursor was drop-casted onto the sample, followed by the placement of a Teflon foil to prevent contact with the mask, which would shadow all areas except the ones of interest in the negative resist. The sample was then exposed for 2 cycles of 60 s in a mask aligner. Removal of

3.5. Experimental Procedure

excess, non-cross-linked precursor was careful blown off with a N₂ gun, as shown in Figure 3.9b, following references [4][41].

OECT with inkjet-printed Solid-State Electrolyte. After the application of the adhesion promoter, the solid-state-electrolyte precursor was ink-jet printed and expose for 2 cycles of 60 s in mask aligner, as illustrated in Figure 3.9c. Parameters and procedure for ink-jet printing was previously established by members of BioSens group at IAPP [42].

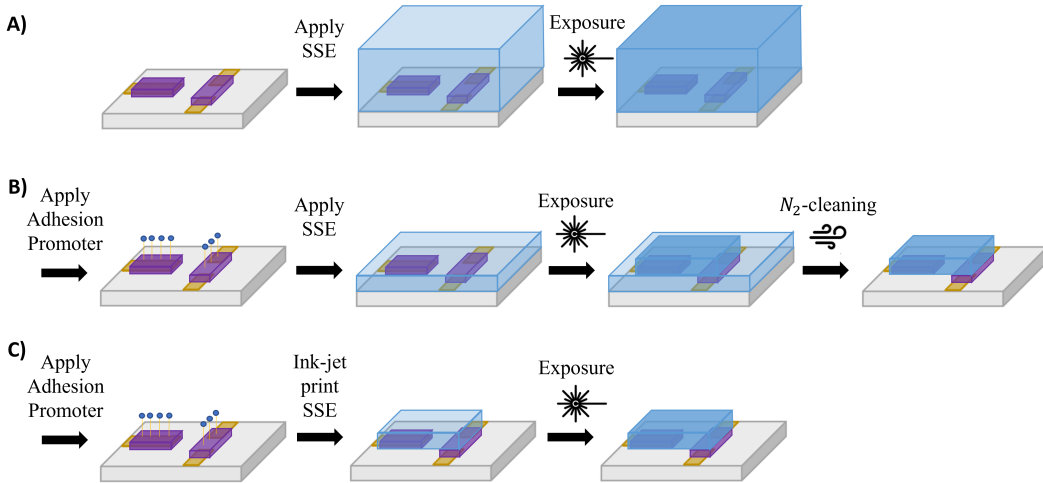


Figure 3.9: Visualization of the workflow for solid-OECT fabrication with undoped p(g3T2-T) by A) drop-casting SSE, B) photopatterning SSE, C) ink-jet printing SSE.

3.5.4.2 Solid-OECTs using Doped-p(g3T2-T)

OECT with inkjet-printed Solid-State Electrolyte. After the deposition of films and dopant (F₆T CNNQ), films were stored in glovebox over the weekend to let dopants soak and dry. Then, the patterning steps for doped-p(g3T2-T) from Subsection 3.5.3.1 were followed with no extra cycles in exposure times. Solid-state electrolyte precursor was ink-jet printed as described in the previous subsection, and depicted in Figure 3.10. Then, transfer characteristics were measured at a constant V_{DS} of -0.1V, and a V_{GS} swept backwards from 1.0 V to 1.0 V at a scanning rate of 0.083 V/s. Cyclic voltammetry and electrochemical impedance spectroscopy were performed by short-circuiting source and drain to probe between channel and gate. Parameters were fixed as described in Section 3.3, and measurements were taken one day after the fabrication.

3. EXPERIMENTAL METHODS

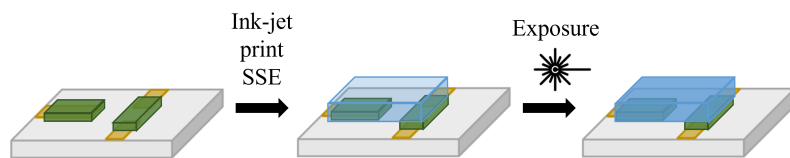


Figure 3.10: Visualization of the workflow for solid-OECT fabrication with doped p(g3T2-T) by ink-jet printing SSE.

Chapter 4

Results and Discussion

4.1 Doping Characterization

After dynamic spin-coating of p(g3T2-T) and F₄TCNQ dopant on top, followed by a subsequent baking step, a visible effect is demonstrated in Figure 4.1, where the reflection hue shifts towards more yellowish tones, as also reported in reference [3].

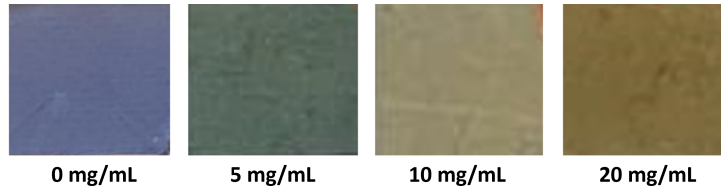


Figure 4.1: Color change upon increasing dopant concentration from 0 to 20 mg/mL.

This color shift is expected as the optical properties of any material change upon doping. The spectra are discussed in more detailed later in this section.

4.1.1 Thickness, Sheet Resistance, and Resistivity

The film thickness was determined through profilometer measurements, resulting in an approximate thickness of 70 nm. Sheet resistance and resistivity were calculated using a four-point probe and the Van Der Pauw method, as shown in Table 4.1. These calculations were performed using equations 3.1 and 3.2, respectively, as described in the previous chapter.

	Undoped	5 mg/mL	10 mg/mL	20 mg/mL
R _S (Ω/sq)	6.3M	104.6k	70.7k	49.4k
ρ (Ωcm)	44.1	0.73	0.49	0.35

Table 4.1: Sheet resistance and resistivity values for undoped and doped films of p(g3T2-T) with F₄TCNQ.

4. RESULTS AND DISCUSSION

Upon doping, a substantial decrease is observed in both sheet resistance and resistivity. However, this decrease is not as pronounced when higher dopant levels are introduced, as depicted in Figure 4.2.

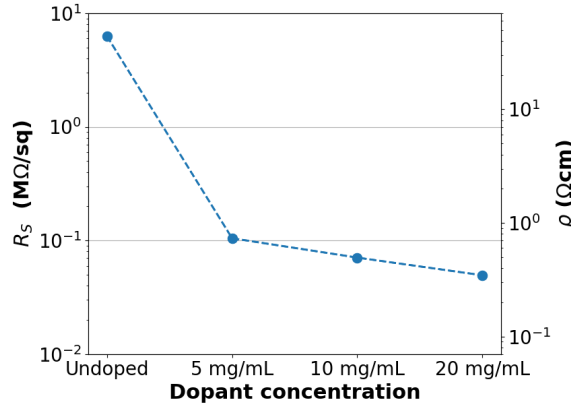


Figure 4.2: Sheet resistance and resistivity drop upon doping of p(g3T2-T) with $F_4\text{TCNQ}$.

4.1.2 Absorbance measurements

The visible color hue shift can be quasi-quantitatively described by examining the absorbance spectra of the samples, as illustrated in Figure 4.3. In the case of undoped p(g3T2-T), there is a prominent absorption peak at 588 nm, which diminishes with increasing doping concentration, indicative of oxidation. Notably, new absorption peaks emerge at around 860 nm, a consequence of polaron generation, leading to new optical transitions, as explained in Section 2.1.2.

Tan et al. documented the appearance of new absorption peaks within the 300 to 600 nm range. The higher energy (lower wavelength) peak is generated by unreacted neutral dopant species (TCNQ^0), while the second is attributed to the new dopant anions (TCNQ^-), which induce charges in our polymer [3]. Additionally, it is worth noting that, after several days of storage, the initially dominant peak of unreacted neutral dopants diminishes in intensity relative to the peak attributed to anions. This observation could be attributed to the ongoing diffusion of dopants through the polymer over time. Another contributing factor could be changes in the morphology. Further measurements are needed to confirm precise dopant concentration in polymer.

Absorbance values are correlated with the density of states of these new optical transitions [11]. In our spectra, the absorbance value at 860 nm of the p(g3T2-T) sample with 5 mg/mL dopant concentration is relatively higher (around 40%) compared to higher dopant levels. This finding might initially appear counterintuitive. However, as the doping concentration increases, the formation of bipolarons and bipolaron bands becomes energetically more favorable [43]. This phenomenon aligns with observations in the higher wavelengths, such as at 1600 nm, where absorbance increases in the more highly doped p(g3T2-T) sample.

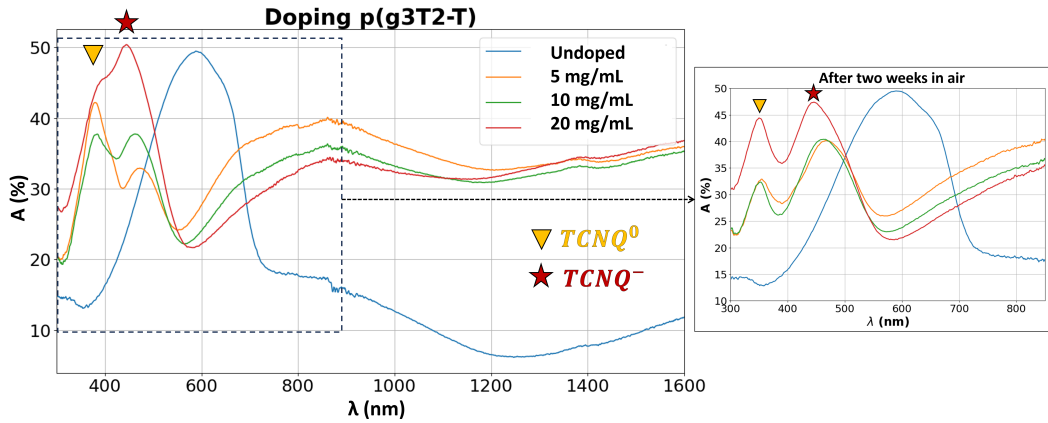


Figure 4.3: Spectra of undoped and doped p(g3T2-T) at different doping levels, corresponding to samples on Figure 4.1. Figure at the right represents absorbance after two weeks of storage in ambient conditions.

Moreover, Tan et al. reported the formation of bipolarons in this specific context, evidenced by a shift to lower energies in the broad absorbance spectrum within the mid-IR region (wavenumbers 1000-1600 cm⁻¹) [3]. Consequently, further analysis of hole bipolaron formation can be conducted with Fourier Transform InfraRed (FTIR) spectroscopy.

4.1.3 Workfunction

In the context of studying electron energy levels in Ultraviolet Photoelectron Spectroscopy (UPS), the ideal film preparation involves working under inert conditions to prevent contamination. However, our current OECT fabrication process unavoidably exposes our films to ambient conditions. Consequently, we conducted measurements following deposition under these ambient conditions. As expected, UPS shows a shift of E_{HBEC} and E_{HOMO} values towards the Fermi level, which, in the material, is equivalent to an increase in the workfunction. This leads to a Fermi level shift towards the HOMO level as the dopant concentration increases, as depicted in Figure 4.4, which is characteristic of p-type doping. Unfortunately, potential contamination issues prevented the measurement of samples with a dopant concentration of 20 mg/mL, but the trend is clearly discernable.

	Undoped	5 mg/mL	10 mg/mL
E_{HBEC} [eV]	17.35	16.47	16.36
E_{HOMO} (vs E_F)	4.28	3.27	3.24
WF [eV]	3.87	4.28	4.86

Table 4.2: Calculated workfunction from UPS measurements and represented in Figure 4.4.

4. RESULTS AND DISCUSSION

It is crucial to recognize that UPS is a surface-sensitive measurement. The penetration depth of the ultraviolet-range photons in UPS is limited to approximately 2 nm, significantly less than the thickness of our polymer film (approximately 70 nm). Consequently, this technique restricts our understanding of the diffusion of dopants throughout the entire volume of the polymer. Although, we gained some insights into this matter in the previous subsection, further analysis could be carried out using UPS with a depth-profiling option.

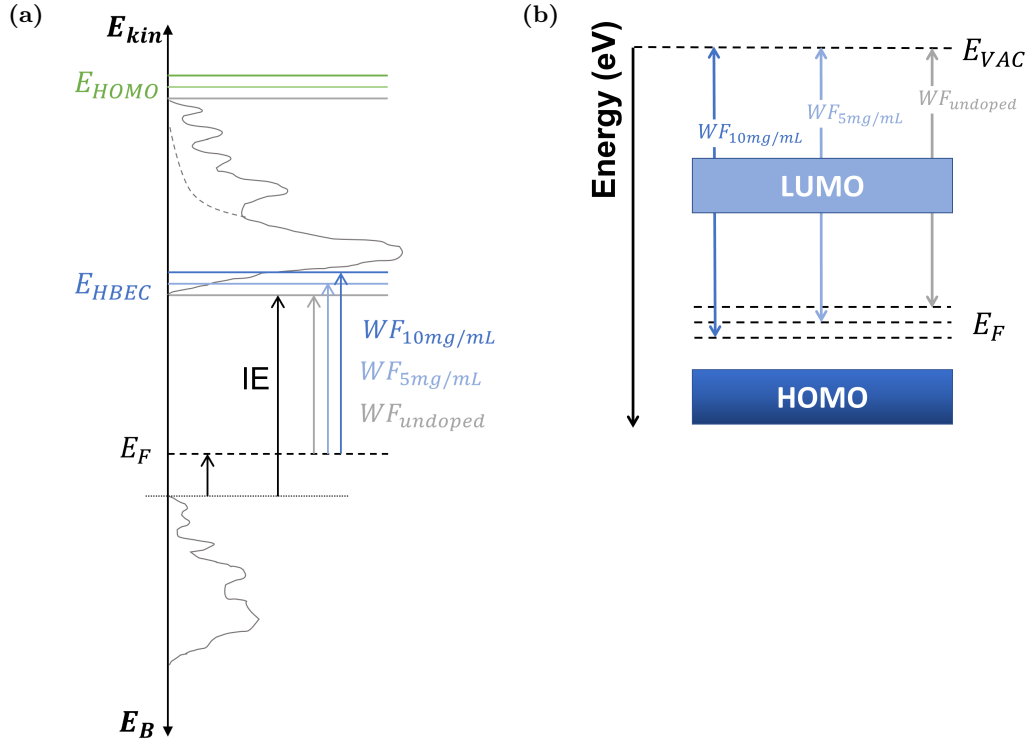


Figure 4.4: Graphical representation of a) the relationship between the binding energies E_B and the kinetic energy of the photoelectrons E_{kin} , and b) the Fermi level shift, upon doping.

4.2 Doping in Organic Electrochemical Transistors

In the previous section, an investigation into doping levels with different F_4TCNQ concentrations was conducted. As expected, the samples exhibited an increase in conductivity, the formation of polarons and bipolarons, and an increase in the workfunction of the material as the dopant concentration increased. Now, our focus shifts to the fabrication of OECTs.

Our ultimate goal is to study fully patterned solid-state OECTs that will enable integrated circuits (IC) and thermodynamic studies [44]. Consequently, it was imperative to initially investigate the isolated impact of channel doping on our

devices. Therefore, as detailed in the previous chapter, we will pair our channel with a non-polarizable gate, such as a Ag/AgCl, a widely used configuration for investigating OECT-based materials. This will be coupled with a Solid-State Electrolyte (SSE) precursor, the specific composition was outlined in Table 3.3 of Chapter 3.

We have formulated two hypotheses, based on reference [3], regarding the expected performance of our devices:

1. Transfer characteristics may be adversely impacted by channel doping.
2. The introduction of ionic species (TCNQ^-) into p(g3T2-T) films should result in depletion-mode devices with positive threshold voltages. This is because a higher positive gate bias would be needed to counteract these anions and turn off the device.

4.2.1 Influence of Doping on OECT Channel

The patterning process was successfully accomplished via photolithography, as detailed in Section 3.5.3.1, employing a mask that included a microstructured gate. This setup is ideal for studying OECTs with both channel and gate constructed from the same OMIEC material, commonly PEDOT:PSS. The result of this process is displayed in Figure 4.5.

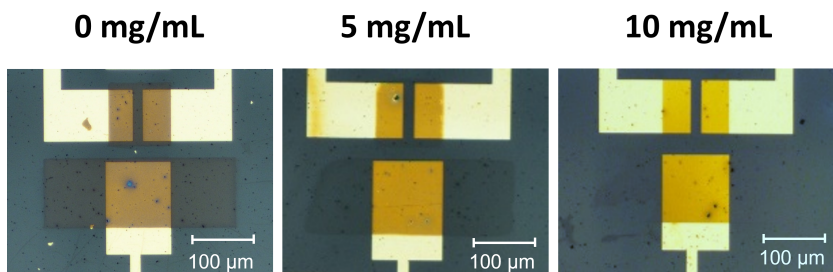


Figure 4.5: Micrographs of patterned channel and gate with p(g3T2-T) undoped, 5 mg/mL and 10 mg/mL dopants, following procedures explained in Section 3.5.3.1.

The results shown in Figures 4.6 - 4.8 correspond to the same device and the same loop on each sample (undoped, 5 mg/mL, and 10 mg/mL dopants) from the same batch of materials. After reporting the analysis of individual devices, a more comprehensive statistical study will be conducted on operational devices from each sample.

It is essential to note that for the statistical analysis of this section, despite our efforts to increase the yields, only 3 or 4 out of the 14 devices were operational in each sample. The undoped polymer exhibited a strong affinity with the photoresist, complicating the development process. Additionally, samples with higher dopant concentrations required longer UV light exposure times, and overdevelopment occurred more frequently, resulting in lower yields. Optimization for specific parts of the process

4. RESULTS AND DISCUSSION

were necessary and ultimately accomplished, and will be detailed in subsequent sections of this chapter.

Transfer characteristics are illustrated in Figure 4.6a, c, e, corresponding to undoped, 5 mg/mL, and 10 mg/mL dopants, respectively. Notably, a positive turn-on voltage is observed in the undoped OECT device, indicating the rapid oxidation (unwanted) of p(g3T2-T) under environmental conditions due to its low ionization potential (IP).

The drain current (I_D) of the undoped device exhibits higher values than doped devices. Hidalgo et al. [45] reported that pristine p(g3T2-T) exhibits a oxygen reduction reaction (ORR) activity in oxygen-saturated conditions, resulting in an increase in current within the polymer until saturation. To address this issue, it will be necessary to control the oxidation state of the polymer during selective steps of the fabrication process or find a way to reverse the oxidation of p(g3T2-T), which will be explored in subsequent sections.

Gate current (I_G) is represented by dotted lines, and it is apparent that the drain OFF current ($I_{D,OFF}$) is dominated by this leakage current in all devices.

$ g_{m,max} $ [mS] @	Undoped	5 mg/mL	10 mg/mL
$V_{DS} = -0.1$ V	0.75	0.45	0.24
$V_{DS} = -0.3$ V	2.01	1.31	0.74
$V_{DS} = -0.5$ V	2.90	1.97	1.09
$V_{DS} = -0.7$ V	3.59	2.23	

Table 4.3: Maximum transconductance values extracted from Figure 4.6

Notably, the device with the highest dopant concentration (10 mg/mL dopant) shows signs of breakage as V_{DS} becomes more negative (Figure 4.6e and Figure 4.7d). Consequently, this measurement will be excluded from the calculation of transconductance and threshold voltage.

Figure 4.7 illustrates that doped devices exhibit minimal differences in $I_{D,OFF}$ but there is a noticeable decrease in $I_{D,ON}$ as the doping levels increase. This is reflected in the maximum transconductance values displayed in Table 4.3, where a clear drop of $|g_{m,max}|$ is evident with increasing doping levels. This outcome aligns with our initial hypothesis and warrants further investigations with impedance measurements to calculate volumetric capacitance.

However, a more striking observation is evident in Figure 4.7 and Figure 4.8: the turn-on voltages and threshold voltages, respectively, **have shifted towards negative values** as the dopant concentration increased in all V_{DS} values, **contradicting our initial hypothesis**. This suggest a kind of “**compensation doping effect**” in the OECTs, which requires further investigation and resolution.

Additionally, threshold voltage values exhibited lower variability among different V_{DS} values with higher doping levels, are depicted in Figure 4.8a. In the undoped device, the variability could be attributed to the ORR, which may differ under different drain bias conditions. In contrast, in the doped devices, this variability is

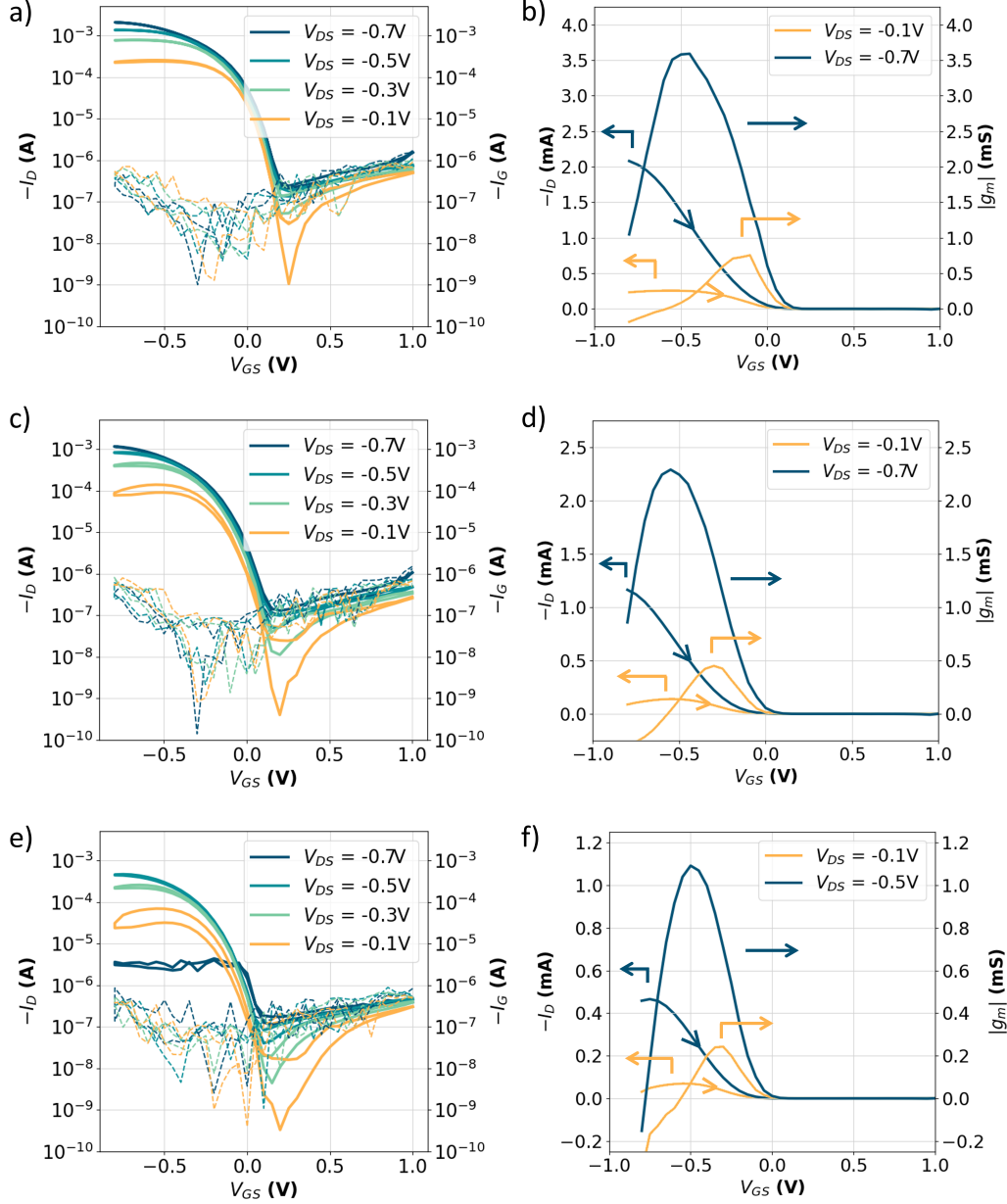


Figure 4.6: a), c) , e) Transfer characteristics of all measured V_{DS} including the gate leakage current I_G b), d), f) Transfer curves (off-switching) with corresponding transconductance. Each group of graphs for undoped and 5 mg/mL and 10 mg/mL doped p(g3T2-T) channel, respectively.

expected to decrease since doping depletes reactive electrons from p(g3T2-T) with F₄TCNQ, ensuring better stability in air [3].

However, the statistical analysis presented in Figure 4.8b aligns with the previous

4. RESULTS AND DISCUSSION

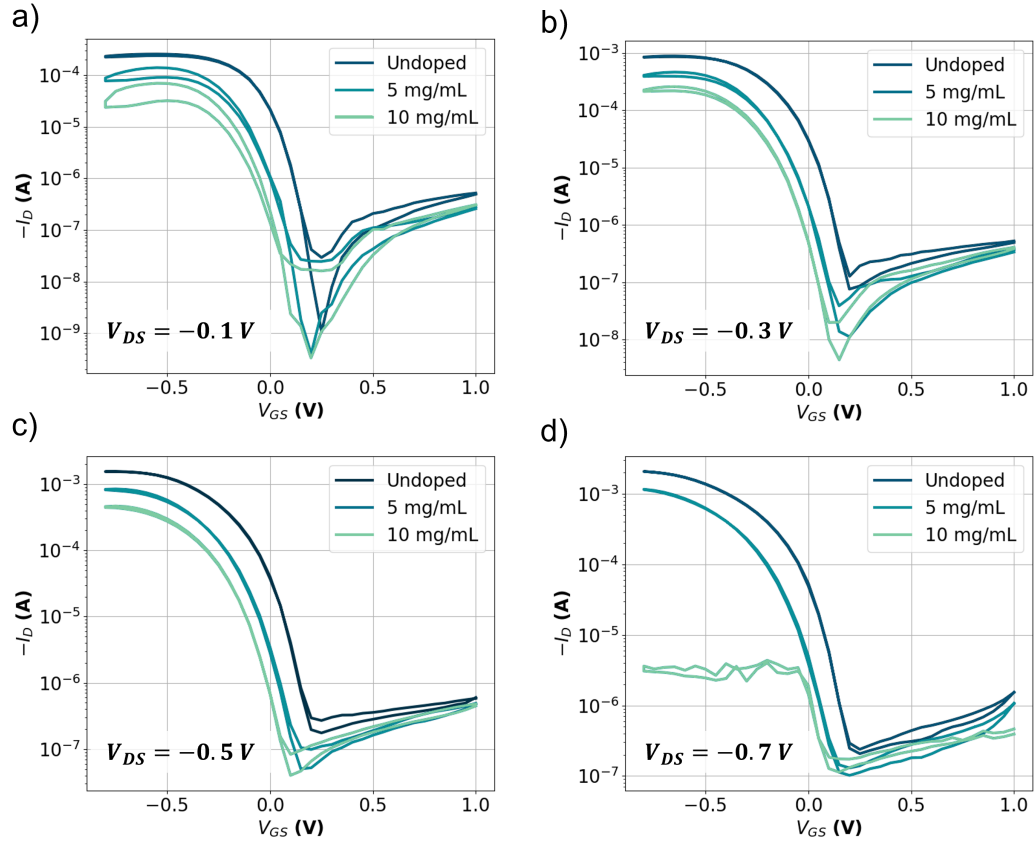


Figure 4.7: Transfer characteristics comparing undoped, 5 mg/mL and 10 mg/mL dopants devices, each graph represent a different V_{DS}

statement for 5 mg/mL dopant concentration only, but not for 10 mg/mL. Some other factors may have intervened such as low degree of homogeneity in doping or patterning defects.

Furthermore, while not presented in this report, it was observed during the analysis that undoped OEET devices exhibit higher repeatability in transfer characteristics as measurement loops increase. The saturation of ORR in undoped species, as mentioned earlier, may contribute to this repeatability. However, the variability in doped species requires further study. For instance, understanding the stability of dopants upon contact with the polymer and the electrolyte would be valuable.

4.2.2 Stability of Undoped and Doped p(g3T2-T)

From the previous subsection, it was concluded that a better understanding of the stability of undoped and doped p(g3T2-T) under ambient conditions, as well as how their electrical properties change upon contact with the SSE precursor, is needed. Consequently, this subsection will focus on monitoring the channel conductivity

4.2. Doping in Organic Electrochemical Transistors

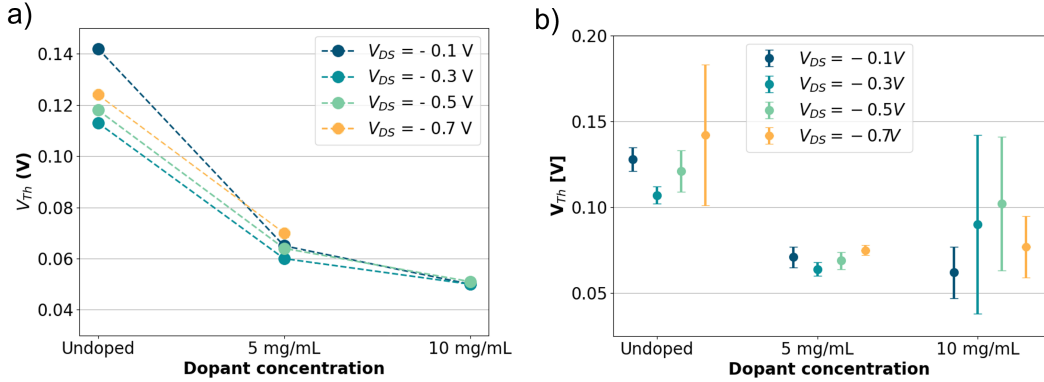


Figure 4.8: Threshold shift at different doping levels and V_{DS} corresponding to a) data shown in Figure 4.6, and b) all operating devices in each sample.

under both N_2 and ambient environments, both before and after contact of SSE precursor.

The channel conductivity of an undoped device was measured immediately after spin-coating, yielding a value of $1 \mu\text{S}$. After undergoing the patterning process described in the previous sections, the conductivity increased three orders of magnitude to approximately 1 mS . Even though, μS values already signify oxidation, the patterning process further oxidizes our material.

Measurements of I_D at V_{DS} of -0.3 V and no gate bias exhibited a small decrease of 4% and small increase of 15% within two hours in N_2 and ambient air environments, respectively. This observation suggests that stability in ambient air is compromised due to unwanted doping.

A similar study was conducted with a doped device containing 5 mg/mL of F_6TCNNQ dopant, resulting a higher level of doping compared to F_4TCNQ at the same concentration, as detailed in Appendix A. The channel conductivity reached a value of $266 \mu\text{S}$ with a reduction of 1.2% within one hour in N_2 environment and remained stable with minimal fluctuations of 1.0% within one hour in ambient condition. This indicates a lower conductivity compared to the oxidized p(g3T2-T) but similar stability in air, as expected from reference [3].

Remarkably, upon contact with SSE precursor, conductivity of both samples drops significantly, approximately six orders of magnitude, in an N_2 environment, reaching the sensitivity limits of our equipment and resulting in a noisy signal, as shown in Figure 4.9a. One plausible explanation is that p(g3T2-T), as a type VI OMIEC, lacks chemical binding with TCNQ^- anions. When in contact with the electrolyte, the anions are drawn away from the polymer backbone (de-doping), restoring its original insulating state. However, it may be possible that cations from the electrolyte could enter the polymer film and neutralize the anions. Further experiments would be needed to clarify both explanations. Either way, having an insulating polymer film is essential for accumulation-mode OECTs.

Under ambient conditions, there is a smaller decrease of slightly more than one

4. RESULTS AND DISCUSSION

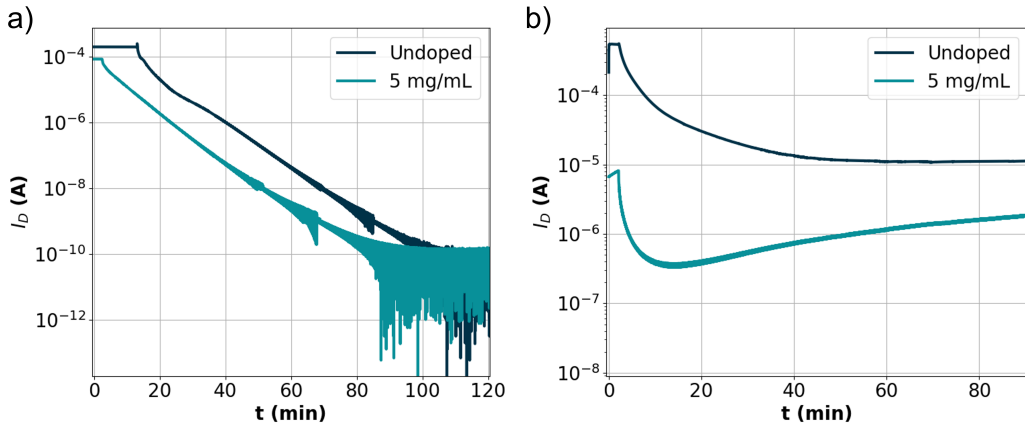


Figure 4.9: Drain current over time of undoped p(g3T2-T) coupled with SSE precursor under a) N_2 , and b) ambient environment.

order of magnitude for the undoped sample, as seen in Figure 4.9b. The doped sample initially exhibited a similar but faster drop within the first 15 minutes, followed by a sudden increase of I_D . In both scenarios, the ORR prevented a greater decrease in current. The fluctuation seen in the doped species may be attributed to the simultaneous occurrence of irreversible de-doping and ORR .

Transfer curves of the undoped device using an Ag/AgCl pellet as gate were measured under ambient conditions after de-doping in N_2 environment, as depicted in Figure 4.10. The device exhibited shifts in its ON voltage and negative threshold voltages values, as summarized in Table 4.4, moving towards negative values. A visible sign of degradation was perceived at the end of the measurements (in this case, when V_{DS} was -0.1 V). This will be further addressed in the next subsection.

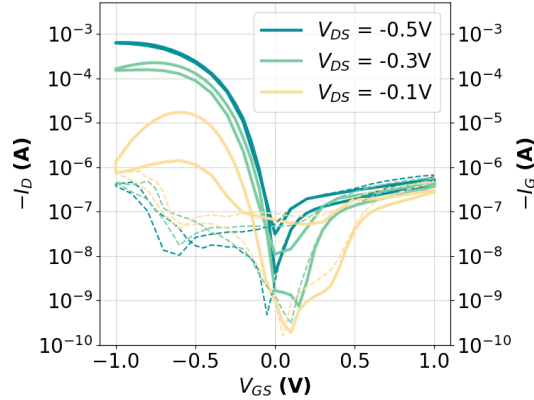


Figure 4.10: Transfer characteristics after electrochemical de-doping at different V_{DS} under ambient conditions. Solid and dashed lines indicate I_D and I_G , respectively.

V_{DS} [V]	V_{Th} [V]
-0.1	-0.18
-0.3	-0.15
-0.5	-0.13

Table 4.4: Threshold voltage extracted from Figure 4.10

In summary, a pre de-doping step could potentially serve as a method for obtaining accumulation-mode OECTs by decreasing the conductivity of p(g3T2-T), and will be explored in the following section.

4.2.3 Counteracting Oxidation by Electrochemical De-doping

Now that we have identified an alternative method to counteract the oxidation of p(g3T2-T), we will proceed with initial trials of accumulation-mode OECT using both the Ag/AgCl gate and the OMIEC gate. Our first step will involve expediting the de-doping process by applying a positive gate bias to one of the devices. This will allow us to achieve low conductivity within a couple of minutes, as opposed to the two hours reported in the previous subsection.

De-doping in a N_2 environment was performed by applying a +1 V gate bias. p(g3T2-T) reached its insulating state in less than 300 seconds, significantly faster than observed in the previous section. However, it was expected that this process would not be reversible upon disconnection of the gate. Figure 4.11a confirms this expectation: after I_D drastically dropped and the gate was disconnected (gray arrows), the current remained low, and leakage current is predominant. When the gate was reconnected (gold arrows), a capacitive current spike occurred but later stabilized to match the leakage current.

Transfer curves using the p(g3T2-T) gate showed a negative turn-on voltage after electrochemical de-doping (Figure 4.11b). Additionally, a transfer curve was measured after exposure to UV light. The monomer units in the SSE (NIPAm and HHPA) cross-link upon exposure forming the polymer poly(N-isopropylacrylamide) (PNIPAm), then an increase in current upon crosslinking is observed.

Moreover, it was perceived that using the OMIEC gate instead of the Ag/AgCl pellet affects our “gating efficiency”, as expected. Weissbach et al. [46] demonstrated the Electrochemical Electrode Coupling (ECC) between channel and its electrode has a more pronounced effect on device operation when micro-integrated polarizable gates (OMIECs) are used. This coupling can result in saturation loss and threshold voltage roll-off when increasing V_{DS} , which was observed during measurements. Therefore, moving forward, V_{DS} will be fixed at -0.1 V.

The subsequent experiment involved exposing the sample to ambient conditions, using the same device that underwent electrochemical de-doping. Unfortunately, it experienced degradation between measurements. Subsequently, transfer characteristics of another device from the same sample were measured using a Ag/AgCl pellet, as depicted in Figure 4.12a. This measurement revealed a negative threshold voltage

4. RESULTS AND DISCUSSION

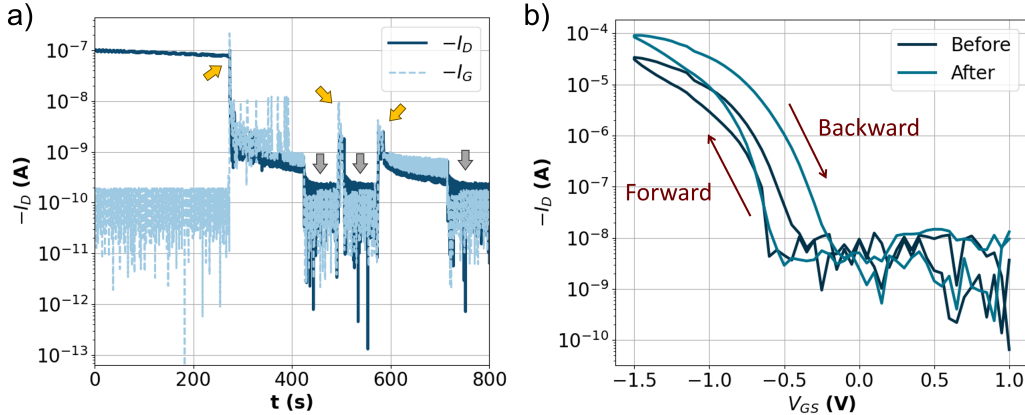


Figure 4.11: a) De-doping p(g3T2-T) using a gate biased of +1V, gold arrows indicate gate connection, while grey arrows indicate when gate was disconnected. b) Transfer characteristic before and after exposure at V_{DS} of -0.1 V using p(g3T2-T) gate coupled with SSE precursor.

of -0.14 V, suggesting that drop-casted SSE, which will be further analyzed in the next section using the p(g3T2-T) gate, may be protecting p(g3T2-T) channel from spontaneous oxidation.

Figure 4.12b shows an increase in gate current from above +0.5 V and below -0.6 V, which is consistent with the increased leakage current in our device. It is important to clarify that the redox peaks extracted from these measurements do not exclusively represent reduction and oxidation potentials between the working electrode (Ag/AgCl) and electrolyte. This is because the counter electrode and reference electrode are shorted and connected to the channel, which should be significantly large to minimize its effects on the electrolyte. Instead, these peaks represent crucial operation points for our OECT, where electron transfer is more pronounced.

For instance, the oxidation peak may signify both the oxidation of the gate and the reduction of the channel, and the same applies to the reduction peaks. This approach will also be used and examined in the next section.

Meanwhile, measurements performed and represented in Figure 4.12c, where Ag/AgCl is now our counter electrode and it is significantly larger than our working electrode (Au/p(g3T2-T) channel), can be correlated with the studies performed by Hidalgo et al. [45], they reported a reduction potential at -0.4 V vs Ag/AgCl attributed to the interactions with molecular oxygen. Therefore, as seen in Subsection 2.3.4, starting from at this operation point, ORR takes place, forming hydrogen peroxide, and leading to degradation, the latter was evident in both devices tested in this subsection.

Although, we are biasing our channel in this trial to values that exceed operational range, this will hold true when using our OMIEC gate.

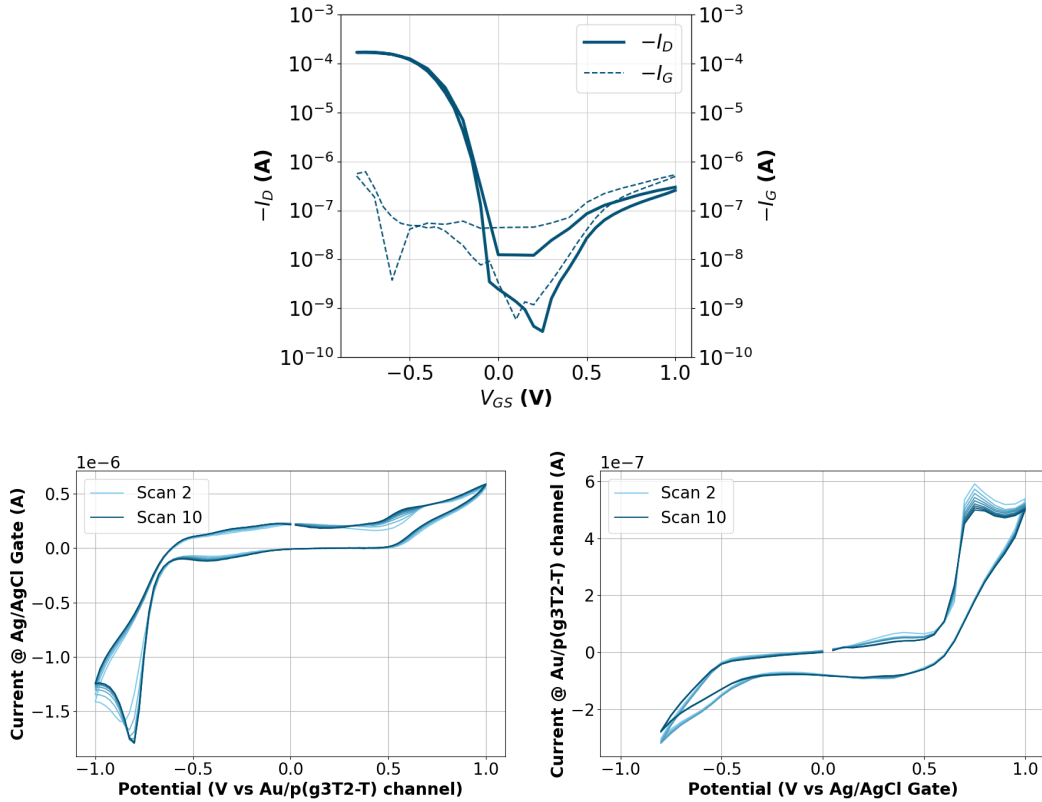


Figure 4.12: a) Transfer characteristics of device using Ag/AgCl gate under ambient conditions, and cyclic voltammograms using Ag/AgCl as b) working electrode and as c) counter electrode shorted with reference electrode.

4.3 Fabrication of Solid Organic Electrochemical Transistors

In the previous section, an investigation into the doping of the p(g3T2-T) channel was conducted, and attention was given to the issues of unwanted oxidation, dopant stability and ORR. With these considerations in mind, the focus now shifts to the fabrication of solid-OECTs.

First, the fabrication of undoped p(g3T2-T) devices will be addressed by simply drop-casting SSE on top of the fourteen pattern devices. With these initial findings, this approach will be refined by structuring the electrolyte by i) photolithography [4] and ii) inkjet printing.

Following the comparison of these three device architectures, doped solid-OECTs will be fabricated, and their threshold voltage shifts upon doping will be evaluated.

4. RESULTS AND DISCUSSION

4.3.1 Undoped Drop-casted SSE

At this point, the patterning process had improved its yield, with twelve out of the fourteen devices being successfully patterned, although there were some variations in thickness, as evidenced by the reflection hue of the micrographs. Among these devices, only seven remained operational.

Electrochemical de-doping of one device in the sample was carried out before exposure. Measurements of channel conductivity of the other devices indicated an impact of this process to neighboring devices (a total of 5) as most of them had very low conductivity, in the order of nS. One exception exhibited a conductivity in the order of μ S and a threshold voltage of 0.0 V. Moreover, attempts to perform irreversible electrochemical de-doping on this device after exposure (cross-linking of monomer units) were unsuccessful. It appeared that the formation of PNIPAm prevented irreversible de-doping. This outcome is crucial for the fabrication of doped-devices and will be discussed further in Section 4.3.4.

Four devices from the sample were measured under the same conditions as detailed in Section 3.5.4.1. A representative device can be seen in Figure 4.13a, note that this sample was used for reverse oxidation experiments, the reflection hue changed from brownish to bluish color after lowering its conductivity. SSE precursor was blew off and a new drop was deposited for the solid-OECT.

Transfer characteristics exhibited a $|g_{m,max}|$ value of 79μ S. Threshold voltages were calculated for forward and backward scans, that led to values of 0.09 V and -0.06 V, respectively, exhibiting a small hysteresis. Further analysis on hysteresis is considered beyond the scope of this work.

Using EIS measurements and fitting into the equivalent circuit model (inset image at Figure 4.13c) lead to $C_{channel}$ of 34.0 nF and C* calculations yield to 36.5 Fcm^{-3} , much lower than the $211 \pm 18 \text{ Fcm}^{-3}$ [26] or 144 Fcm^{-3} [45] reported in the literature.

Furthermore, cyclic voltammograms exhibit major oxidation and reduction peaks of +0.65 V and -0.08 V, respectively, with a smaller but significant reduction peaks at -0.32 V and oxidation peak at -0.01 V. Redox potentials close to the turn-on voltage values in this device can be correlated with the low hysteresis observed in transfer characteristics: Appendix B shows how a device with some fabrication defects showing a large hysteresis on the transfer characteristics.

The major reduction peak, on the other hand, occurs when device is at the OFF state, no major changes are perceived in I_D , but a big decrease in I_G . Additionally, from our observations from Subsection 4.2.3, the presence of redox potentials outside the turn-on voltages observed in both the channel and gate may indicate the occurrence of ORR in our device due to the remaining degree of oxidation in both our channel and gate. Further experiments are needed to confirm this hypothesis. For instance, cyclic voltammetry measurements under controlled oxygen-saturated environments should be conducted using an ideal electrical configuration, including a large counter electrode and a separate reference electrode.

A statistical analysis on the four devices are shown in Table 4.5. Most importantly, negative threshold voltages were calculated. Additionally, all exhibited the same

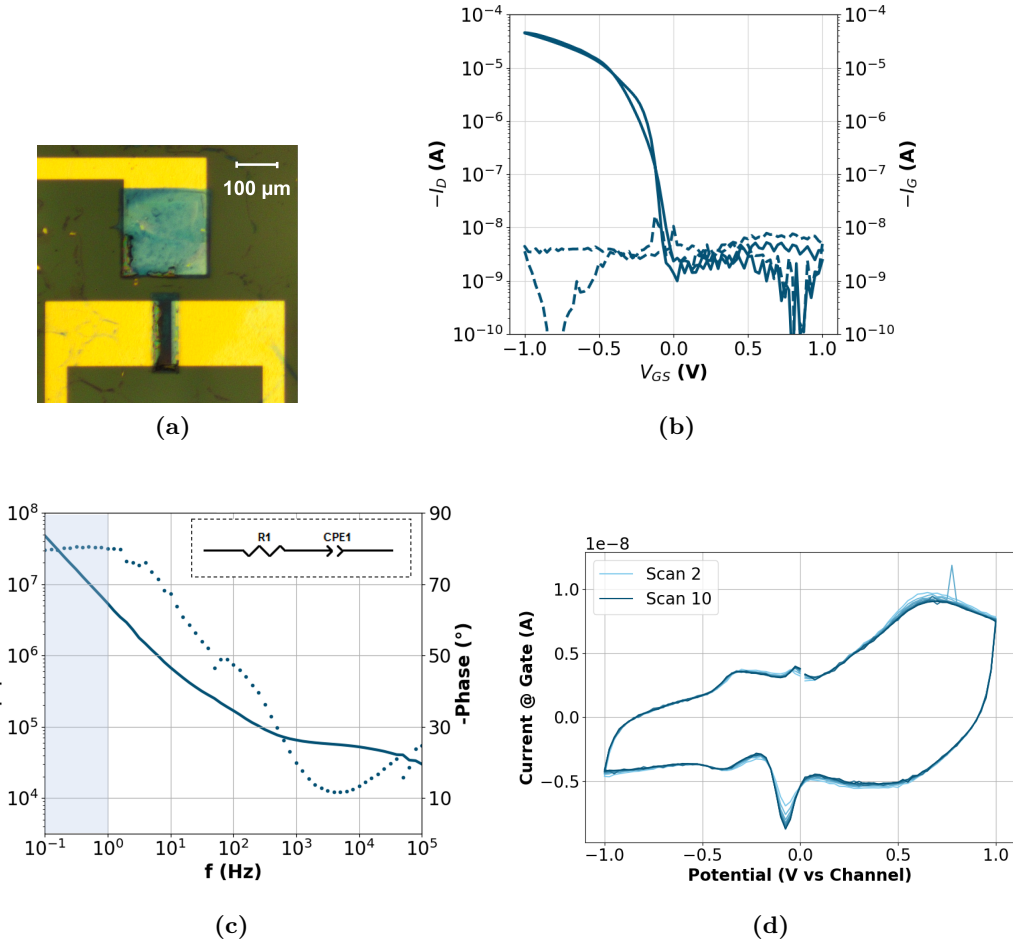


Figure 4.13: a) Micrograph of patterned device before application of SSE, b) transfer characteristics at V_{DS} of -0.1 V. And representative c) Bode plot obtained by EIS and d) cyclic voltammograms.

prominent oxidation peak (0.68 ± 0.02 V), but only peaks close to the turn-on voltages are reported.

4.3.2 Undoped Photopatterned SSE

This trial resulted in ten out of fourteen operational devices. However, certain devices exhibited unusual behavior due to defects, or some SSE partially removed from the device. These devices were excluded from the analysis, leaving us with a total of seven devices.

The microstructuring of SSE on top of the OMIEC channel and gate required the use of an adhesion promoter, which differs from the drop-casted SSE. In this particular case, the removal of non-crosslinked SSE precursor was achieved using a

4. RESULTS AND DISCUSSION

Parameters	Value	Parameters	Value
$V_{Th,forward}$ [V]	-0.30 ± 0.13	$V_{Th,backward}$ [V]	-0.17 ± 0.08
$C_{channel}$ [nF]	40.9 ± 12.2	C^* [Fcm $^{-3}$]	43.9 ± 13.1
V_{ox} [V]	-0.33 ± 0.05	V_{red} [V]	-0.42 ± 0.19

Table 4.5: Parameters extracted from the characterization of drop-casted SSE OECTs

N_2 gun, using an adhesion promoter reduces the risk of removing crosslinked SSE. Moreover, the application of the adhesion promoter was followed by an ethanol rinsing and high-temperature baking steps at 100°C, as explained in Subsection 3.5.4. Both of these steps helped to reverse the oxidation of the polymer. Ethanol initiates a reaction with oxygen as described below:



The baking step evaporates the water content in the polymer formed by the reaction. Therefore, electrochemical de-doping before SSE patterning was not necessary. This approach will be used for the following samples.

A representative device can be seen in Figure 4.14a, device exhibit signs of oxidation indicated by the brownish hue. Micrograph was taken before the application of the adhesion promoter.

Transfer characteristics, depicted in Figure 4.14b, exhibited a $|g_{m,max}|$ value of 139 μ S. Threshold voltages of -0.10 V and -0.18 V for forward and backward scans, respectively, with a small hysteresis.

From the EIS results shown in Figure 4.14c, a $C_{channel}$ of 34.5 nF and C^* of 37.0 Fcm $^{-3}$ were calculated. Cyclic voltammograms gave prominent oxidation and reduction peaks of +0.03 V and -0.20 V, respectively, closer to turn-on voltages, as seen in Figure 4.14d, with smaller, but significant oxidation peaks at -0.32 V and +0.57 V.

A statistical analysis of all devices is shown in Table 4.6. Importantly, negative threshold voltages were calculated, although not as negative as the electrochemical de-doping ones from previous subsection.

Parameters	Value	Parameters	Value
$V_{Th,forward}$ [V]	-0.08 ± 0.05	$V_{Th,backward}$ [V]	-0.09 ± 0.04
$C_{channel}$ [nF]	51.1 ± 17.7	C^* [Fcm $^{-3}$]	54.9 ± 19.0
V_{ox} [V]	-0.01 ± 0.20	V_{red} [V]	-0.11 ± 0.09
$ g_{m,max} $ [μ S]	107 ± 162		

Table 4.6: Parameters extracted from the characterization of photopatterned SSE OECT under N_2 environment.

Regarding cyclic voltammograms, only redox peaks close to turn-on voltages are

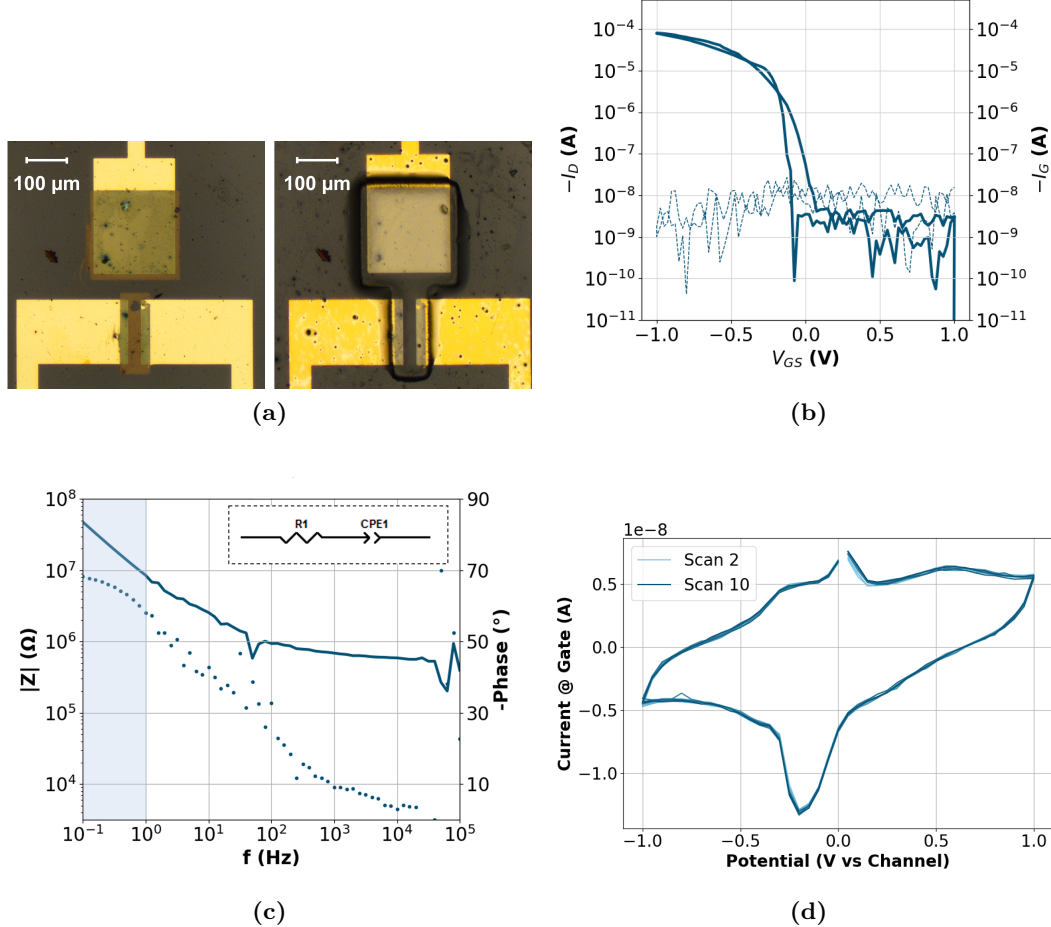


Figure 4.14: a) Micrograph of patterned device before and after application of SSE, b) transfer characteristics at V_{DS} of -0.1 V. And representative c) Bode plot obtained by EIS and d) cyclic voltammograms.

reported, which were not necessarily the most prominent ones, unlike representative device. Another identified oxidation potential in all devices was 0.46 ± 0.09 V, which falls within the values identified in the previous device configuration (drop-casted SSE).

The channel and volumetric capacitance show a clear increase compared to drop-casted SSE, possibly due to persistent degree of oxidation of p(g3T2-T) that enhances channel conductivity.

Upon exposure to ambient environment conditions, measurements revealed depletion-mode devices with a positive turn-on and threshold voltages, as depicted in transfer characteristics shown in Figure 4.15a. This suggests that, unlike drop-casted SSE, photopatterned SSE does not provide sufficient “shielding” to prevent oxidation of p(g3T2-T).

4. RESULTS AND DISCUSSION

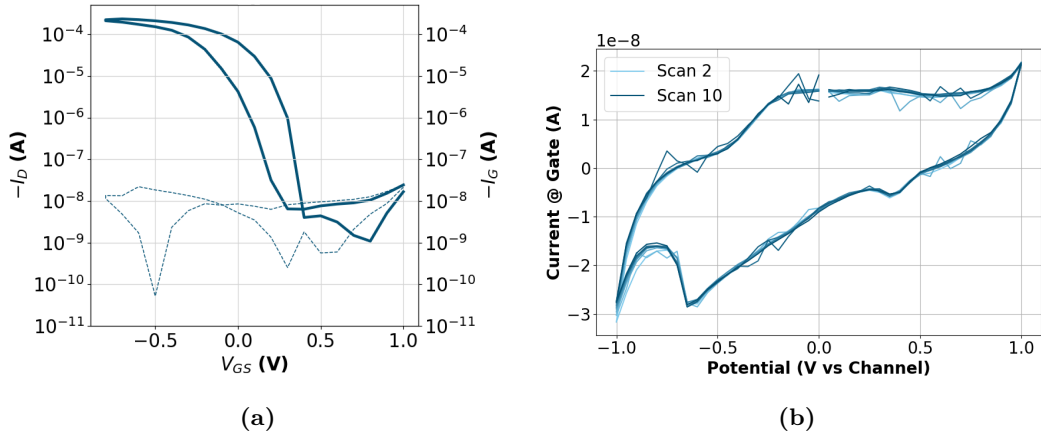


Figure 4.15: a) Transfer characteristics at V_{DS} of -0.1 V, and b) cyclic voltammograms, of same device from Figure 4.14

Calculated parameters of operational devices exposed to ambient conditions are shown in Table 4.7, an increase on transconductance compared to the N_2 environment condition is perceived, which aligns with the increase in current due to oxidation. The reported redox potentials represent the potential values close to the turn-on voltages, again they may not necessarily correspond to the most prominent peaks. Although the average redox values showed no hysteresis, differences were observed in most devices and in the transfer curves.

Interestingly, devices exhibited prominent peak at -0.37 ± 0.08 V and -0.56 ± 0.09 V in the oxidation and reduction scans, respectively suggesting complex electrochemical processing occurring in our devices. While the oxidation of the polymer is evident, the occurrence of ORR and the generation of hydrogen peroxide cannot be ruled out during operation. These redox peaks could represent a more complex scenario where ORR is initiated either by the electrochemically doped p(g3T2-T) channel or by the biased p(g3T2-T) gate. Again, further controlled experiments are needed to confirm this hypothesis.

Parameters	Value	Parameters	Value
$V_{Th,forward}$ [V]	0.36 ± 0.05	$V_{Th,backward}$ [V]	0.25 ± 0.13
V_{ox} [V]	0.40 ± 0.11	V_{red} [V]	0.40 ± 0.09
$ g_{m,max} $ [μ S]	315 ± 44		

Table 4.7: Parameters extracted from the characterization of photopatterned SSE OECT under ambient conditions

4.3.3 Undoped Inkjet-Printed SSE

While photopatterned SSE offered an approach to obtain microstructuring devices with high yields and relatively good performances, the removal of non-crosslinked SSE is not as efficient, the method potentially leaves residual material that can lead to device crosstalk and leakage. Ink-jet printing represents a promising approach to address this limitation [42]. However, to ensure good printing, the adhesion promoter step remains crucial and, as commented before, aids in reversing the oxidation of p(g3T2-T).

For this trial, patterning process yielded a total of seven devices. However, issues with film uniformity resulted in only four devices being successfully printed. This may have been caused by contamination or improper coating of the adhesion promoter. Among these four devices, only one was fully operational, and it will be used in the subsequent analysis.

The printing process takes approximately two hours per sample under ambient conditions. Efforts were made to set the printing parameters using a different sample while subjecting our device to high temperatures and ethanol rinsing. Unfortunately, the resulting device still exhibited signs of oxidation, as will be shown in the analysis.

Figure 4.16 illustrates all the mentioned measurements, and Table 4.8 presents the calculated parameters. Threshold voltages calculated between scans show minimal difference, indicating almost no hysteresis, so only one value is reported. Importantly, V_{Th} is no longer negative; there is a shift towards positive values (oxidation), resulting in a higher transconductance.

The channel capacitance and volumetric capacitance also exhibit an increase in value, which is reflected in higher I_{ON} . Furthermore, cyclic voltammograms show predominant peaks close to the turn-on voltages but also secondary peaks in the oxidation scan at -0.33 V and +1.0 V, and in the reduction scan at -0.55 V.

Parameters	Value	Parameters	Value
V_{Th} [V]	0.13	$ g_{m,max} $ [μ S]	355
$C_{channel}$ [nF]	85.3	C^* [Fcm $^{-3}$]	91.6
V_{ox} [V]	0.15	V_{red} [V]	0.09

Table 4.8: Parameters extracted from the characterization of printed SSE OEET

In conclusion, it appears that the undoped p(g3T2-T) sample is not compatible with the printed SSE process. Its extended exposure time to environmental conditions, leading to unavoidable oxidation, prevents the attainment of an accumulate-mode OEET. New methods to counteract this oxidation are needed if printed SSE is to be used, or photolithography should be considered, despite the possible device crosstalk.

4.3.4 Doped Inkjet-Printed SSE

Doped p(g3T2-T) has been demonstrated to be stable under ambient conditions, and owing to the advantages of printed SSE, this method will be the chosen approach for

4. RESULTS AND DISCUSSION

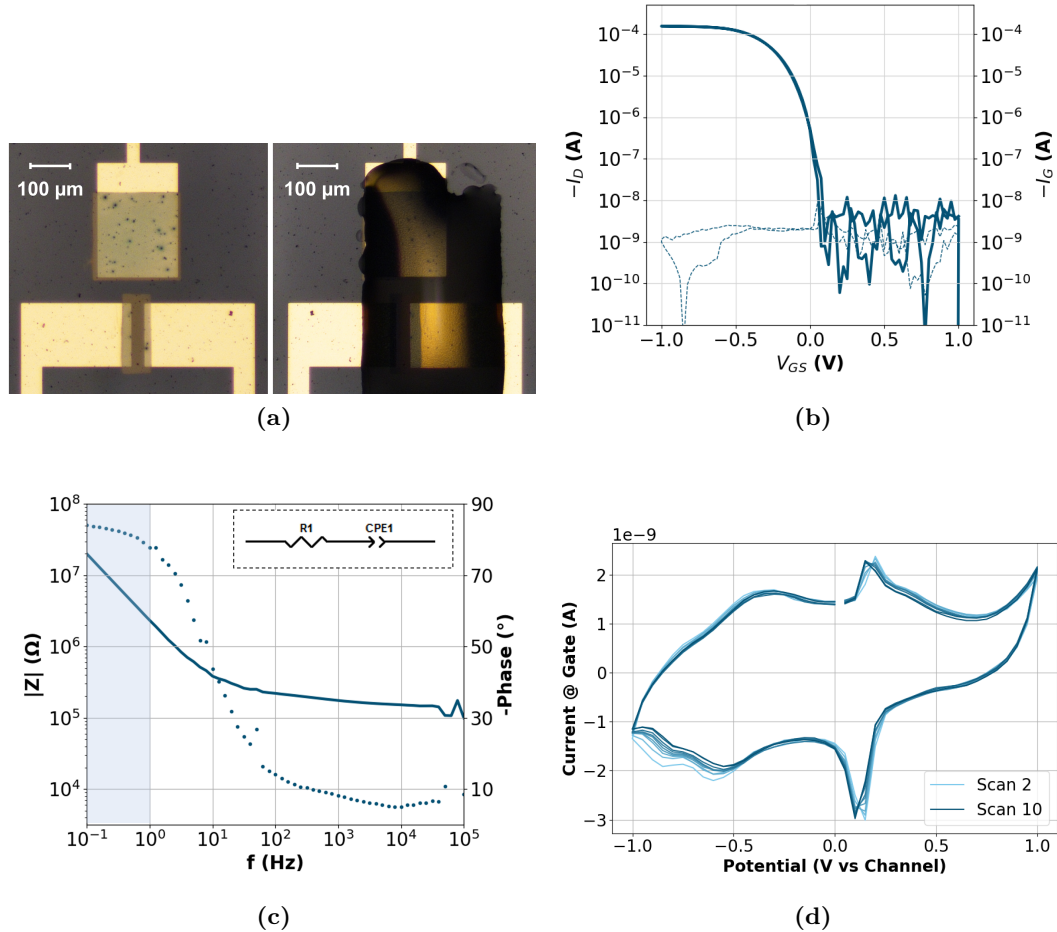


Figure 4.16: a) Micrograph of patterned device with printed SSE, b) transfer characteristics at V_{DS} of -0.1 V. c) Bode plot obtained by EIS and d) cyclic voltamograms.

SSE application in this subsection.

Different doping levels were intended to be studied in this subsection. However, only 5 mg/mL of F₆T CNNQ resulted in doping homogeneity suitable for meaningful comparison with undoped p(g3T2-T). Figure 4.17 reveals irregularities in doping when using a new vial of 10 mg/mL dopant concentration, and the same issue was observed for vials prepared with 15 mg/mL dopant. Acetonitrile was unable to correctly dissolve this dopant at high concentrations, which was not observed with F₄T CNNQ and one initial vial of 10 mg/mL F₆T CNNQ. Consequently, achieving depletion-mode OECTs with higher and homogeneous doping levels was not possible.

From the experiments conducted with undoped p(g3T2-T) in Subsection 4.2.3, it was observed that upon UV light exposure, the electrochemical de-doping of a device was no longer irreversible. Therefore, as a first step, the channel conductivity

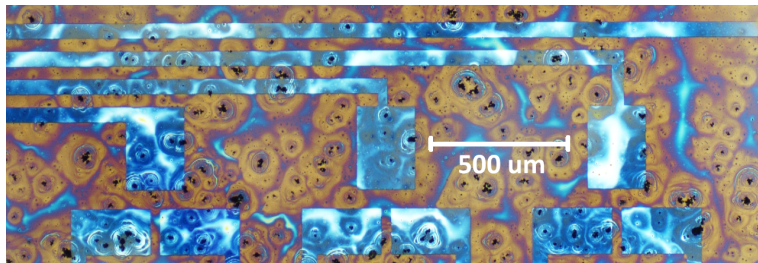


Figure 4.17: Micrograph of inhomogeneous doping in sample.

was monitored with SSE on top. The sample with 5 mg/mL dopant maintained a conductivity of 4 μ S for two hours with some fluctuation and approximately 10% drop in conductivity. While some conductivity was lost, it was not a significant drop of orders of magnitude.

The adhesion promoter used for undoped p(g3T2-T) could not be used for doped species since it will remove dopants during the application steps. An alkaline adhesion promoter would be needed, which required additional experiments to test its effectiveness and correct application. Therefore, no promoter was used at this stage, so low yields in printing were expected, despite the high yields in patterning.

Eight operational devices were obtained. However, only one exhibited a capacitive behavior that allowed for the measurement of transfer characteristics, and it will be used in this analysis. Transfer characteristics, EIS, and CV measurements are shown in Figure 4.18, and the calculated parameters are exhibited in Table 4.9.

Despite the use of doped p(g3T2-T), the threshold voltage remains slightly negative. A positive shift has been achieved when compared with undoped p(g3T2-T) with the lowest conductivity. However, the shift achieved by oxidized p(g3T2-T) is significantly higher.

It is important to note that it is not certain that this value corresponds to the mentioned doping level. This uncertainty arises because under ambient conditions, doped p(g3T2-T) upon contact with SSE precursor, experiences a significant drop in conductivity within the first 15 minutes at V_{DS} of -0.1 V, as discussed in Subsection 4.2.2. Therefore, during the time between the printing process and the crosslinking of SSE, it is possible that this effect took place in our device, albeit at a lower rate since it was not biased. Further experiments are needed to confirm this hypothesis.

A noisy EIS spectrum was obtained, possibly due to environmental factor or a defect in the gate electrode that is perceived in the micrograph. Calculations of the channel and volumetric capacitance was made using the dotted line, where an expected trend was identified. High channel capacitance and volumetric capacitance were calculated, as expected, but new devices are needed to confirm this value.

Additionally, cyclic voltammograms show predominant peaks close to turn-on voltages but also secondary peaks in the oxidation scan at -0.25 and +1.0 V, and in the reduction scan at -0.33 V.

4. RESULTS AND DISCUSSION

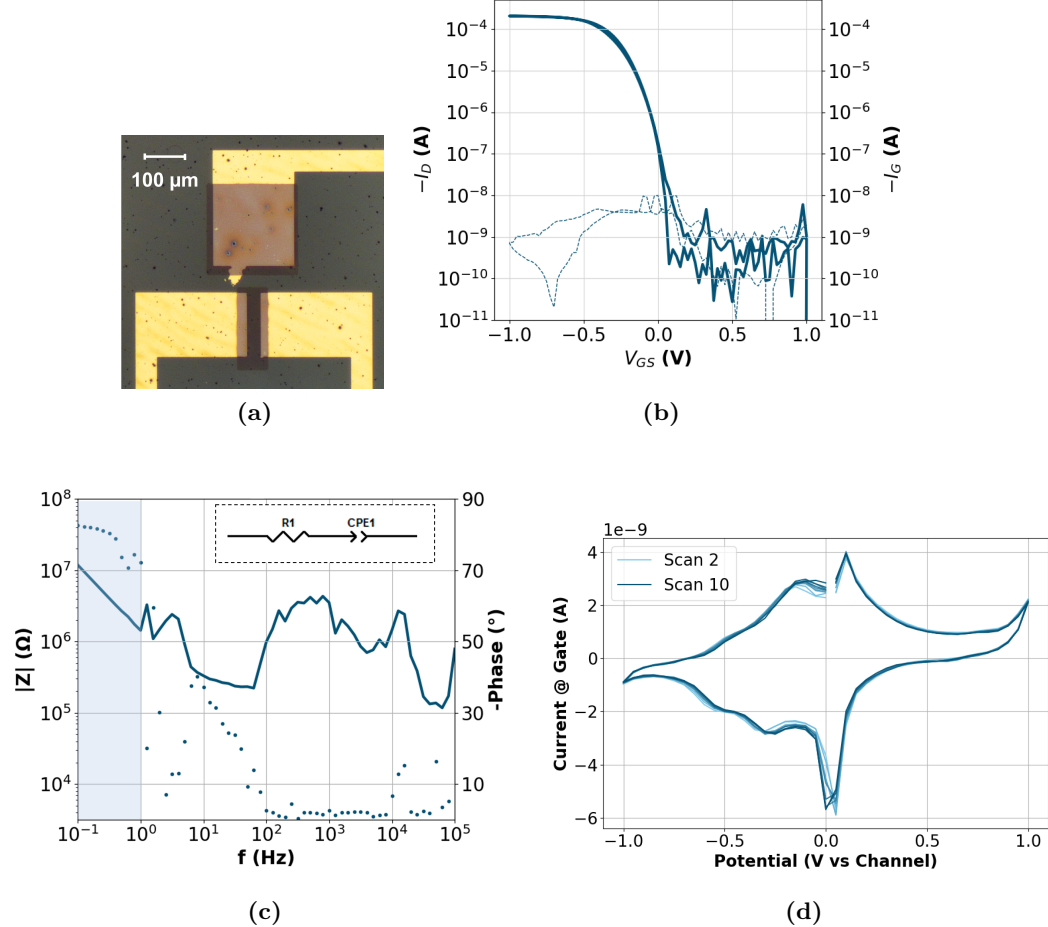


Figure 4.18: a) Micrograph of patterned device with printed SSE, b) transfer characteristics at V_{DS} of -0.1 V. c) Bode plot obtained by EIS and d) cyclic voltamograms.

4.3.5 Threshold Voltage Shift in OECTs

Having performed individual analysis of each fabricated device, including important OECT figures of merit such as transconductance, volumetric capacitance and redox potentials, our focus in this subsection is now on the threshold voltage and, more importantly, the expected shift upon doping.

Figure 4.19 exhibits the threshold voltage of all operating devices for each sample described in this section.

It was found that electrochemical de-doping of p(g3T2-T) prior exposure to UV light of the SSE precursor produced the most negative threshold voltages, although with high variability. This may be attributed to various factors, such as devices not being directly impacted by the electrochemical de-doping (only one device is de-doped

4.3. Fabrication of Solid Organic Electrochemical Transistors

Parameters	Value	Parameters	Value
V_{Th} [V]	-0.10	$ g_{m,max} $ [μS]	567
$C_{channel}$ [nF]	130	C^* [Fcm^{-3}]	140
V_{ox} [V]	0.10	V_{red} [V]	0.0

Table 4.9: Parameters extracted from the characterization of doped-p(g3T2-T) OECT

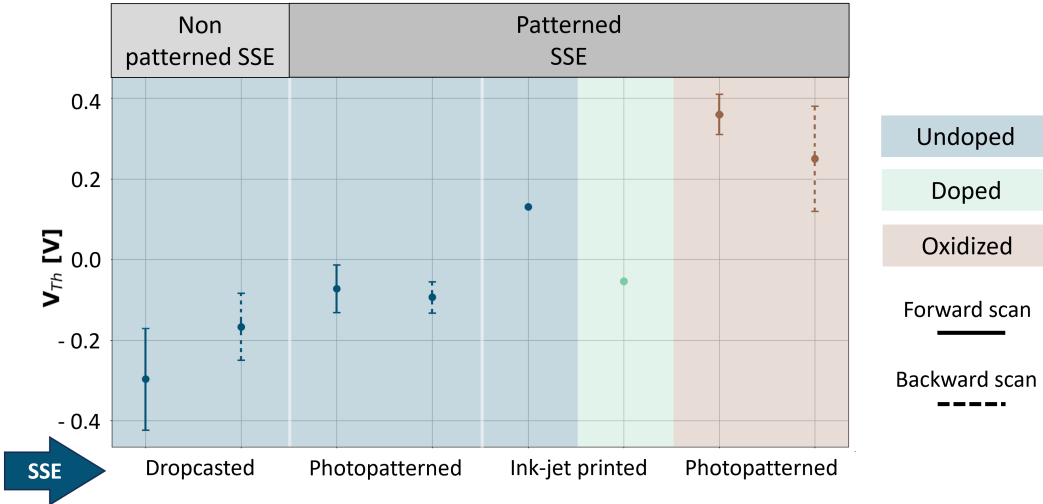


Figure 4.19: Threshold voltage of all studies samples including error bars from operating device in each group.

and not included in this calculation), resulting in different degrees of de-doping, or defect within the photolithography process.

More importantly, the device fabricated using p(g3T2-T) doped with 5 mg/mL F₆T CNNQ dopant concentration exhibits a threshold voltage that is slightly shifted towards positive values, the unwanted oxidation of p(g3T2-T) with molecular oxygen achieves positive values more effectively, allowing the fabrication of accumulation-mode OECTs. The cause of the low threshold voltage shift was previously discussed, and it is likely due to the extended time between printing and exposure, during which TCNNQ⁻ anions may be drawn away to the SSE or compensation doping occurs upon contact with SSE precursor during the printing process. In either case, further studies are necessary to determine which hypothesis is more accurate in order to counteract this effect. For the former, an adhesion promoter before the application of dopants may be a possible solution. Additionally, applying photopatterned SSE may yield better results, as the effect will still occur but time between application and exposure is much shorter.

Chapter 5

Conclusions and Outlook

Appendix A

Absorption of p(g3T2-T) Doped with F6TCNNQ

Appendix B

Correlation of Cyclic Voltammetry and Transfer Characteristics

Appendix C

PEDOT:PSS vs Doped p(g3T2-T) as Channel

Bibliography

- [1] J. Rivnay, S. Inal, A. Salleo, R. M. Owens, M. Berggren, and G. G. Malliaras, “Organic electrochemical transistors,” *Nature Reviews Materials*, vol. 3, no. 2, pp. 1–14, 2018.
- [2] C. B. Nielsen, A. Giovannitti, D.-T. Sbircea, E. Bandiello, M. R. Niazi, D. A. Hanifi, M. Sessolo, A. Amassian, G. G. Malliaras, J. Rivnay, and I. McCulloch, “Molecular Design of Semiconducting Polymers for High-Performance Organic Electrochemical Transistors,” *Journal of the American Chemical Society*, vol. 138, no. 32, pp. 10 252–10 259, 2016.
- [3] S. T. M. Tan, G. Lee, I. Denti, G. LeCroy, K. Rozylowicz, A. Marks, S. Griggs, I. McCulloch, A. Giovannitti, and A. Salleo, “Tuning Organic Electrochemical Transistor Threshold Voltage using Chemically Doped Polymer Gates,” *Advanced Materials*, vol. 34, no. 33, p. 2202359, 2022.
- [4] A. Weissbach, L. M. Bongartz, M. Cucchi, H. Tseng, K. Leo, and H. Kleemann, “Photopatternable solid electrolyte for integrable organic electrochemical transistors: Operation and hysteresis,” *Journal of Materials Chemistry C*, vol. 10, no. 7, pp. 2656–2662, 2022.
- [5] L. Alcácer, *Electronic Structure of Organic Semiconductors: Polymers and Small Molecules*. Morgan & Claypool Publishers, Dec. 2018.
- [6] A. J. Heeger, S. Kivelson, J. R. Schrieffer, and W. P. Su, “Solitons in conducting polymers,” *Reviews of Modern Physics*, vol. 60, no. 3, pp. 781–850, Jul. 1988.
- [7] M. Heydari Gharahcheshmeh and K. K. Gleason, “Texture and nanostructural engineering of conjugated conducting and semiconducting polymers,” *Materials Today Advances*, vol. 8, p. 100086, Dec. 2020.
- [8] J. L. Bredas, B. Themans, J. M. Andre, R. R. Chance, and R. Silbey, “The role of mobile organic radicals and ions (solitons, polarons and bipolarons) in the transport properties of doped conjugated polymers,” *Synthetic Metals*, vol. 9, no. 2, pp. 265–274, Apr. 1984.
- [9] B. Lüssem, M. Riede, and K. Leo, “Doping of organic semiconductors,” *physica status solidi (a)*, vol. 210, no. 1, pp. 9–43, 2013.

BIBLIOGRAPHY

- [10] M. L. Tietze, L. Burtone, M. Riede, B. Lüssem, and K. Leo, “Fermi level shift and doping efficiency in \$p\$-doped small molecule organic semiconductors: A photoelectron spectroscopy and theoretical study,” *Physical Review B*, vol. 86, no. 3, p. 035320, Jul. 2012.
- [11] J. L. Bredas and G. B. Street, “Polarons, bipolarons, and solitons in conducting polymers,” *Accounts of Chemical Research*, vol. 18, no. 10, pp. 309–315, Oct. 1985.
- [12] D. Kiefer, R. Kroon, A. I. Hofmann, H. Sun, X. Liu, A. Giovannitti, D. Stegerer, A. Cano, J. Hyynnen, L. Yu, Y. Zhang, D. Nai, T. F. Harrelson, M. Sommer, A. J. Moulé, M. Kemerink, S. R. Marder, I. McCulloch, M. Fahlman, S. Fabiano, and C. Müller, “Double doping of conjugated polymers with monomer molecular dopants,” *Nature Materials*, vol. 18, no. 2, pp. 149–155, Feb. 2019.
- [13] M. T. Fontana, D. A. Stanfield, D. T. Scholes, K. J. Winchell, S. H. Tolbert, and B. J. Schwartz, “Evaporation vs Solution Sequential Doping of Conjugated Polymers: F₄TCNQ Doping of Micrometer-Thick P3HT Films for Thermoelectrics,” *The Journal of Physical Chemistry C*, vol. 123, no. 37, pp. 22 711–22 724, Sep. 2019.
- [14] I. E. Jacobs, E. W. Aasen, J. L. Oliveira, T. N. Fonseca, J. D. Roehling, J. Li, G. Zhang, M. P. Augustine, M. Mascal, and A. J. Moulé, “Comparison of solution-mixed and sequentially processed P3HT:F4TCNQ films: Effect of doping-induced aggregation on film morphology,” *Journal of Materials Chemistry C*, vol. 4, no. 16, pp. 3454–3466, Apr. 2016.
- [15] S. T. M. Tan, “Organic Mixed Ionic Electronic Conductors for Electrochemical Devices,” Ph.D. dissertation, Stanford University, Palo Alto, CA, Dec. 2022.
- [16] A. Giovannitti, R. B. Rashid, Q. Thiburce, B. D. Paulsen, C. Cendra, K. Thorley, D. Moia, J. T. Mefford, D. Hanifi, D. Weiyuan, M. Moser, A. Salleo, J. Nelson, I. McCulloch, and J. Rivnay, “Energetic Control of Redox-Active Polymers toward Safe Organic Bioelectronic Materials,” *Advanced Materials*, vol. 32, no. 16, p. 1908047, 2020.
- [17] G. A. Snook, P. Kao, and A. S. Best, “Conducting-polymer-based supercapacitor devices and electrodes,” *Journal of Power Sources*, vol. 196, no. 1, pp. 1–12, Jan. 2011.
- [18] Y. Liang, Z. Tao, and J. Chen, “Organic Electrode Materials for Rechargeable Lithium Batteries,” *Advanced Energy Materials*, vol. 2, no. 7, pp. 742–769, 2012.
- [19] B. D. Paulsen, K. Tybrandt, E. Stavrinidou, and J. Rivnay, “Organic mixed ionic–electronic conductors,” *Nature Materials*, vol. 19, no. 1, pp. 13–26, Jan. 2020.

- [20] S. Wang, M. Ha, M. Manno, C. Daniel Frisbie, and C. Leighton, “Hopping transport and the Hall effect near the insulator–metal transition in electrochemically gated poly(3-hexylthiophene) transistors,” *Nature Communications*, vol. 3, no. 1, p. 1210, Nov. 2012.
- [21] S. T. M. Tan, A. Gumyusenge, T. J. Quill, G. S. LeCroy, G. E. Bonacchini, I. Denti, and A. Salleo, “Mixed Ionic–Electronic Conduction, a Multifunctional Property in Organic Conductors,” *Advanced Materials*, vol. 34, no. 21, p. 2110406, 2022.
- [22] J. T. Friedlein, R. R. McLeod, and J. Rivnay, “Device physics of organic electrochemical transistors,” *Organic Electronics*, vol. 63, pp. 398–414, Dec. 2018.
- [23] D. A. Bernards and G. G. Malliaras, “Steady-State and Transient Behavior of Organic Electrochemical Transistors,” *Advanced Functional Materials*, vol. 17, no. 17, pp. 3538–3544, 2007.
- [24] S. Inal, G. G. Malliaras, and J. Rivnay, “Benchmarking organic mixed conductors for transistors,” *Nature Communications*, vol. 8, no. 1, p. 1767, Nov. 2017.
- [25] S. T. Keene, T. P. A. van der Pol, D. Zakhidov, C. H. L. Weijtens, R. A. J. Janssen, A. Salleo, and Y. van de Burgt, “Enhancement-Mode PEDOT:PSS Organic Electrochemical Transistors Using Molecular De-Doping,” *Advanced Materials*, vol. 32, no. 19, p. 2000270, 2020.
- [26] M. Moser, L. R. Savagian, A. Savva, M. Matta, J. F. Ponder, T. C. Hidalgo, D. Ohayon, R. Hallani, M. Reisjalali, A. Troisi, A. Wadsworth, J. R. Reynolds, S. Inal, and I. McCulloch, “Ethylene Glycol-Based Side Chain Length Engineering in Polythiophenes and its Impact on Organic Electrochemical Transistor Performance,” *Chemistry of Materials*, vol. 32, no. 15, pp. 6618–6628, 2020.
- [27] D. Moia, A. Giovannitti, A. A. Szumska, I. P. Maria, E. Rezasoltani, M. Sachs, M. Schnurr, P. R. F. Barnes, I. McCulloch, and J. Nelson, “Design and evaluation of conjugated polymers with polar side chains as electrode materials for electrochemical energy storage in aqueous electrolytes,” *Energy & Environmental Science*, vol. 12, no. 4, pp. 1349–1357, 2019.
- [28] D. Ohayon, V. Druet, and S. Inal, “A guide for the characterization of organic electrochemical transistors and channel materials,” *Chemical Society reviews*, vol. 52, no. 3, pp. 1001–1023, 2023.
- [29] T. Nguyen-Dang, K. Harrison, A. Lill, A. Dixon, E. Lewis, J. Vollbrecht, T. Hachisu, S. Biswas, Y. Visell, and T.-Q. Nguyen, “Biomaterial-Based Solid-Electrolyte Organic Electrochemical Transistors for Electronic and Neuromorphic Applications,” *Advanced Electronic Materials*, vol. 7, no. 12, p. 2100519, 2021.

BIBLIOGRAPHY

- [30] A. Savva, R. Hallani, C. Cendra, J. Surgailis, T. C. Hidalgo, S. Wustoni, R. Sheelamanthula, X. Chen, M. Kirkus, A. Giovannitti, A. Salleo, I. McCulloch, and S. Inal, “Balancing Ionic and Electronic Conduction for High-Performance Organic Electrochemical Transistors,” *Advanced Functional Materials*, vol. 30, no. 11, p. 1907657, 2020.
- [31] A. Savva, C. Cendra, A. Giugni, B. Torre, J. Surgailis, D. Ohayon, A. Giovannitti, I. McCulloch, E. Di Fabrizio, A. Salleo, J. Rivnay, and S. Inal, “Influence of Water on the Performance of Organic Electrochemical Transistors,” *Chemistry of Materials*, vol. 31, no. 3, pp. 927–937, Feb. 2019.
- [32] P. S. Foundation, “Miscellaneous operating system interfaces,” 2001-2023, date last access: 30-May-2023. [Online]. Available: <https://docs.python.org/3/library/os.html>
- [33] ———, “Csv file reading and writing,” 2001-2023, date last access: 30-May-2023. [Online]. Available: <https://docs.python.org/3/library/csv.html>
- [34] N. Developers, “Numpy user guide,” 2008 - 2022, date last access: 30-May-2023. [Online]. Available: <https://numpy.org/doc/stable/user/index.html#user>
- [35] T. S. community, “Scipy.stats.linregress,” 2008-2023, date last access: 30-May-2023. [Online]. Available: <https://docs.scipy.org/doc/scipy/reference/generated/scipy.stats.linregress.html>
- [36] G. avhn, “Peak detect library,” 2022, date last access: 30-May-2023. [Online]. Available: <https://github.com/avhn/peakdetect/blob/master/README.md>
- [37] J. Hunter, D. Dale, E. Firing, M. Droettboom, and M. development team, “Matplotlib: Quick start guide,” 2012 - 2023, date last access: 30-May-2023. [Online]. Available: https://matplotlib.org/stable/tutorials/introductory/quick_start.html
- [38] S. GmbH, “Sheet resistance calculator,” 2023, date last access: 30-May-2023. [Online]. Available: <https://www.suragus.com/en/technology/sheet-resistance-calculator/>
- [39] E. V. I. for Speciation Analysis (EVISA), “Instrument database: Shimadzu europe - solidspec-3700/3700duv,” 2003-2010, date last access: 30-May-2023. [Online]. Available: <https://speciation.net/Database/Instruments/Shimadzu-Europe/SolidSpec37003700DUV-;i1305>
- [40] S. A. Buchholtz, “Doping Properties of Novel Dopants for Organic Hole Transport Layers,” Master’s thesis, Technische Universität Dresden, Dresden, Germany, nov 2021.
- [41] L. M. Bongartz, “Organic electrochemical transistors with solid-state electrolytes,” Master’s thesis, Technische Universität Dresden, Dresden, Germany, Jul. 2021.

BIBLIOGRAPHY

- [42] H. Tseng, A. Weissbach, J. Kucinski, A. Solgi, R. Nair, L. M. Bongartz, G. Cicccone, M. Cucchi, K. Leo, and H. Kleemann, “Threshold Voltage Control in Dual-Gate Organic Electrochemical Transistors,” *Advanced Materials Interfaces*, vol. 10, no. 19, p. 2201914, 2023.
- [43] C. Enengl, S. Enengl, S. Pluczyk, M. Havlicek, M. Lapkowski, H. Neugebauer, and E. Ehrenfreund, “Doping-induced absorption bands in P3HT: Polarons and bipolarons,” *ChemPhysChem*, vol. 17, no. 23, pp. 3836–3844, 2016.
- [44] M. Cucchi, A. Weissbach, L. M. Bongartz, R. Kantelberg, H. Tseng, H. Kleemann, and K. Leo, “Thermodynamics of organic electrochemical transistors,” *Nature Communications*, vol. 13, no. 1, p. 4514, Aug. 2022.
- [45] T. C. Hidalgo Castillo, M. Moser, C. Cendra, P. D. Nayak, A. Salleo, I. McCulloch, and S. Inal, “Simultaneous Performance and Stability Improvement of a p-Type Organic Electrochemical Transistor through Additives,” *Chemistry of Materials*, vol. 34, no. 15, pp. 6723–6733, Aug. 2022.
- [46] A. Weissbach, M. Cucchi, H. Tseng, K. Leo, and H. Kleemann, “Unraveling the Electrochemical Electrode Coupling in Integrated Organic Electrochemical Transistors,” *Advanced Functional Materials*, p. 2302205, Jul. 2023.